Summer Enhancement of Arctic Sea Ice Volume Anomalies in the September-Ice Zone

MITCHELL BUSHUK

Atmospheric and Oceanic Sciences Program, Princeton University, Princeton, New Jersey

RYM MSADEK

CECI UMR 5318, CNRS/CERFACS, Toulouse, France

MICHAEL WINTON

NOAA/Geophysical Fluid Dynamics Laboratory, Princeton, New Jersey

GABRIEL A. VECCHI

NOAA/Geophysical Fluid Dynamics Laboratory, and Atmospheric and Oceanic Sciences Program, Princeton University, Princeton, New Jersey

RICH GUDGEL, ANTHONY ROSATI, AND XIAOSONG YANG

NOAA/Geophysical Fluid Dynamics Laboratory, Princeton, New Jersey

(Manuscript received 23 June 2016, in final form 8 December 2016)

ABSTRACT

Because of its persistence on seasonal time scales, Arctic sea ice thickness (SIT) is a potential source of predictability for summer sea ice extent (SIE). New satellite observations of SIT represent an opportunity to harness this potential predictability via improved thickness initialization in seasonal forecast systems. In this work, the evolution of Arctic sea ice volume anomalies is studied using a 700-yr control integration and a suite of initialized ensemble forecasts from a fully coupled global climate model. This analysis is focused on the September sea ice zone, as this is the region where thickness anomalies have the potential to impact the SIE minimum. The primary finding of this paper is that, in addition to a general decay with time, sea ice volume anomalies display a summer enhancement, in which anomalies tend to grow between the months of May and July. This summer enhancement is relatively symmetric for positive and negative volume anomalies and peaks in July regardless of the initial month. Analysis of the surface energy budget reveals that the summer volume anomaly enhancement is driven by a positive feedback between the SIT state and the surface albedo. The SIT state affects surface albedo through changes in the sea ice concentration field, melt-onset date, snow coverage, and ice thickness distribution, yielding an anomaly in the total absorbed shortwave radiation between May and August, which enhances the existing SIT anomaly. This phenomenon highlights the crucial importance of accurate SIT initialization and representation of ice–albedo feedback processes in seasonal forecast systems.

1. Introduction

The rapid loss of Arctic sea ice has the potential to influence the climate system across a broad range of spatial and temporal scales. These impacts include changes in the global energy balance via the sea ice–albedo feedback (Budyko 1969; Curry et al. 1995), potential influence on

Supplemental information related to this paper is available at the Journals Online website: http://dx.doi.org/10.1175/JCLI-D-16-0470.s1.

Corresponding author e-mail: Mitch Bushuk, mbushuk@princeton.edu

DOI: 10.1175/JCLI-D-16-0470.1

midlatitude weather (Screen and Simmonds 2013), and many human-related consequences, including the livelihoods of northern communities and Arctic wildlife, the opening of trans-Arctic shipping routes, and new opportunities for resource industries (Jung et al. 2016). The combination of a negative sea ice trend (Stroeve et al. 2012), climate and weather implications, and diverse stakeholder interest has created a burgeoning research focus on the prediction and predictability of Arctic sea ice.

Current seasonal prediction systems based on initialized forecasts made with coupled dynamical models have skill in predicting pan-Arctic sea ice extent (SIE) at lead times of 2–6 months, depending on the initial month and model used (Wang et al. 2013; Chevallier et al. 2013; Sigmond et al. 2013; Merryfield et al. 2013; Msadek et al. 2014; Peterson et al. 2015). These skill estimates are based on retrospective forecasts (hindcasts) that span a significant portion of the satellite era. A larger set of forecasts, spanning 2008 to present, has been collected as part of the sea ice outlook (SIO; Stroeve et al. 2014a), which solicits forecasts of September SIE from dynamical, statistical, and heuristic prediction systems. The SIO predictions have lower skill than the hindcast experiments, which may reflect a general property of seasonal prediction systems (Wang et al. 2010) or may suggest that the present-day Arctic has lower intrinsic predictability than earlier decades (Blanchard-Wrigglesworth et al. 2015). Importantly, the forecast skill in both the hindcast experiments and the SIO is substantially lower than the potential predictability of Arctic SIE as estimated by perfect model ensemble experiments. These perfect model experiments, which examine how well a model can predict itself, show that pan-Arctic SIE is potentially predictable at lead times of 12–24 months (Koenigk and Mikolajewicz 2009; Holland et al. 2011; Blanchard-Wrigglesworth et al. 2011b; Tietsche et al. 2014; Germe et al. 2014). These estimates represent an upper limit to sea ice prediction skill, as the forecast errors can be directly attributed to chaotic error growth arising from the nonlinear dynamics of the system. Forecast skill in operational prediction systems is further degraded by errors in initial conditions and model physics. The current gap between potential and operational prediction skill represents an opportunity for improved predictions via improved initialization and model physics.

A key aspect in improving seasonal forecasts is understanding the physical mechanisms that underlie the inherent predictability of Arctic sea ice. Ensuring accurate representation of these mechanisms in forecast systems may be one route to closing the prediction skill gap. Persistence of SIE anomalies has been long recognized as an important source of Arctic predictability (Walsh and Johnson 1979; Lemke et al. 1980). In addition to a persistence of 2–5 months, more recent work has shown that SIE and sea ice concentration (SIC) anomalies exhibit a reemergence of correlation (Blanchard-Wrigglesworth et al. 2011a; Day et al. 2014b; Bushuk et al. 2014, 2015; Bushuk and Giannakis 2015). Specifically, melt-season SIE and SIC anomalies tend to reemerge the following growth season, and growth-season anomalies tend to reemerge the following melt season. Reemergence mechanisms, related to sea surface temperature (SST) and sea level pressure (SLP) regime persistence, and sea ice thickness (SIT) persistence have been proposed for these two reemergence phenomena, respectively. The SST and SLP reemergence mechanisms are relevant for winter sea ice prediction, whereas the SIT mechanism is relevant for summer prediction (Bushuk and Giannakis 2017, manuscript submitted to *J. Climate*).

Other studies have also shown that SIT is an important source of predictability for summer sea ice (Chevallier and Salas y Mélia 2012) and, moreover, that the intrinsic predictability of sea ice may vary with the SIT state, with thick states being more predictable than thin states (Holland et al. 2011; Germe et al. 2014). The multiyear persistence of sea ice volume and SIT anomalies (Day et al. 2014b) implies that knowledge of the SIT state in the preceding winter and spring may be a crucial factor in predicting September SIE. Indeed, a number of recent studies have found that improved SIT initialization leads to improvements in forecast skill on time scales of days (Yang et al. 2014) to seasons (Lindsay et al. 2012; Day et al. 2014a; Collow et al. 2015; Guemas et al. 2016). The lack of pan-Arctic SIT observations has been a past limitation in sea ice prediction efforts; however, the recent *CryoSat-2* and *Soil Moisture and Ocean Salinity* (*SMOS*) satellite SIT measurements (Kaleschke et al. 2012; Laxon et al. 2013; Tilling et al. 2015), which have data coverage in the melt-pond-free months of October through April, represent a new opportunity for accurate, observation-based initialization of SIT.

Another key mechanism affecting summer Arctic sea ice is the positive feedback between SIC and surface albedo, which is a contributor to Arctic amplification of surface warming (Holland and Bitz 2003; Winton 2006). The surface albedo in the Arctic exhibits a complex evolution through the melt season, involving a progression from dry snow-covered ice to ice that is covered by melt ponds (Perovich et al. 2007; Perovich and Polashenski 2012). Subtle changes to this albedo evolution have important implications for the surface energy budget of the Arctic (Serreze et al. 2007) and, hence, the summer melt of sea ice (Stroeve et al. 2014b). Recent work, using a sea ice model that directly simulates surface melt ponds, has identified a strong relationship between spring melt-pond coverage and September SIE (Schröder et al. 2014).

In this study, we draw a connection between SIT-based predictability and surface-albedo-based predictability. Motivated by the need to understand the potential impact of SIT initialization on seasonal prediction skill, we study the temporal evolution of Arctic sea ice volume anomalies, with particular focus on their influence on September SIE. We consider anomalies in the ''September-ice zone,'' the region where September sea ice is typically present, as this is the spatial region where SIT anomalies have greatest potential to affect September SIE. This study is based on analysis of a 700-yr control integration and a suite of initialized forecast ensembles from a fully coupled atmosphere–land–ocean–sea ice model, as described in section 2. In section 3, we document a summer enhancement of sea ice volume anomalies that occurs in the September-ice zone. We find that this summer volume anomaly enhancement is driven by an SIT-state-dependent albedo feedback, in which high- (low-) thickness states drive positive (negative) surface albedo anomalies. In section 4, we examine the details of this mechanism by analyzing the surface energy budget and the factors influencing surface albedo. We find that the summer volume enhancement can be explained by anomalies in absorbed shortwave radiation. These albedo-driven shortwave anomalies are dominated by SIC, surface melt, and snow cover in May and June and by SIC alone in July and August. In section 5, we demonstrate that a similar volume enhancement occurs in initialized ensemble experiments with perturbed SIT initial conditions. Finally, the implications of this phenomenon for seasonal prediction systems are discussed and conclusions are presented in sections 5b and 6, respectively.

2. Model experiments

a. Control integration

This study is based on analysis of a 700-yr control integration of a fully coupled global climate model (GCM) developed at the Geophysical Fluid Dynamics Laboratory (GFDL). The model is based upon the GFDL Climate Model, version 2.5 (CM2.5; Delworth et al. 2012), but employs a lower resolution in the ocean and sea ice components. This model, whose computational efficiency makes it appealing for forecasting applications involving ensembles, is referred to as the Forecast-Oriented Low Ocean Resolution (FLOR) version of CM2.5 (Vecchi et al. 2014). The FLOR model has fully coupled atmosphere, land, ocean, and sea ice components, with nominal horizontal resolutions of 0.5°, 0.5°, 1°, and 1°, respectively. The simulation considered here is a 1990 control run, forced with prescribed 1990-level radiative forcings and run for 1400 years. We use the final 700 years of the run, as the first 700 years show drift associated with model spinup. For all variables considered in this study, the final 700 years of the simulation evolve in a statistically steady state. All data used in this study are monthly averaged.

The sea ice model in the FLOR model is the Sea Ice Simulator, version 1 (SIS1; Delworth et al. 2006). SIS1 uses an elastic–viscous–plastic rheology for the sea ice dynamics (Hunke and Dukowicz 1997), an ice thickness distribution with five thickness categories (Bitz et al. 2001), and a three-layer thermodynamic formulation with one snow layer and two ice layers (Winton 2000). Of particular interest for this study is the treatment of surface albedo in the sea ice model. The model has specified albedo values for dry ice and snow ($\alpha_{\text{ice,dry}}$ = 65% and $\alpha_{\text{snow,dry}}$ = 85%) and wet ice and snow ($\alpha_{\text{ice,wet}}$ = 57.5% and $\alpha_{\text{snow,wet}}$ = 72.7%). The model uses a simple parameterization for surface albedo that is designed to capture the implicit effects of melt ponds (see section 3.6.2 of Hunke et al. 2015). This parameterization determines the surface albedo as a function of the surface skin temperature T_s and the freezing temperature of sea ice T_f, which has a fixed value of −0.054°C in the model. For both snow and ice, the temperature-dependent albedo $\alpha(T_s)$ is given by

$$\alpha(T_s) = \begin{cases} \alpha_{\text{dry}}, & T_s \le -1 + T_f \\ \alpha_{\text{dry}} - (\alpha_{\text{dry}} - \alpha_{\text{wet}})(T_s + 1 - T_f), & -1 + T_f \le T_s \le T_f \\ \alpha_{\text{wet}}, & T_s = T_f, \end{cases} \tag{1}$$

which provides a linear interpolation between the dry and wet albedo values for temperatures within 1°C of T_f.

The model's surface albedo is also directly influenced by the sea ice thickness through the following relation:

$$f_h = \min\left[\frac{\arctan(5h_i)}{\arctan(5\times 0.5)}, 1\right];$$
$$\alpha = f_h\alpha_{\text{ice}} + (1 - f_h)\alpha_{\text{ocean}}, \quad (2)$$

where h_i is the ice thickness (measured in meters) in the ith ice-thickness category, $\alpha_{\text{ocean}} = 6\%$ is the ocean albedo, and $f_h \in [0, 1]$ is the weighting factor for a convex sum between the ice and ocean albedo values. This relation acts to reduce the albedo of ice that is thinner than 0.5 m and leaves the albedo of ice thicker than 0.5 m unchanged.

b. Initialized prediction experiments

We also perform initialized prediction ensemble experiments with the FLOR model. These 12-member ensembles are initialized using an ensemble Kalman filter coupled data assimilation system (ECDA; Zhang et al. 2007), which assimilates surface and subsurface ocean data and atmospheric reanalysis data from the National Centers for Environmental Prediction. The ocean and sea ice initial conditions are taken from ECDA, while the land and atmosphere initial conditions are produced from a suite of AMIP-style atmosphere–land simulations forced by observed SST and sea ice. This method is used to initialize the atmosphere and land components because the FLOR model uses a higher resolution in these components than ECDA, which was built on the CM2.1 model (Delworth et al. 2006). A suite of retrospective initialized FLOR model forecasts spanning 1982–2014 has skill in predicting pan-Arctic SIE at leads of 2–6 months, depending on the initial month (Msadek et al. 2014).

The SIT initial conditions from ECDA are biased thin relative to the FLOR model's free-running model climatology (Msadek et al. 2014) and the available satellite observations of SIT (Tilling et al. 2015). Motivated by this, we perform a set of ensemble predictions with improved SIT initialization. The modified SIT initial conditions use an ECDA SIT anomaly field (computed relative to the ECDA climatology) and add this anomaly to the SIT climatology from the FLOR model (see section b in the appendix for a detailed description). This approach is designed to improve the SIT mean state while retaining the crucial interannual and intra-annual variability captured by the data assimilation procedure. We perform ensemble experiments, termed $\text{FLOR}_{\text{SITpert}}$, for four start dates (1 January, 1 February, 1 March, and 1 April 2013), each consisting of 12 ensemble members. Comparing these to the original prediction experiments from the FLOR model allows us to assess the impact of the modified SIT initial conditions.

3. Summer volume enhancement in the September-ice zone

a. The September-ice zone

The SIT field in the central Arctic crucially affects September SIC, as this thickness field determines how much energy will be required to melt sea ice during the summer months. Since SIT anomalies are persistent on seasonal time scales, winter and spring SIT may be an important source of predictability for September SIE. Winter and spring SIT anomalies may also potentially encode the spatial patterns of future September SIC anomalies (Rigor and Wallace 2004; Williams et al. 2016), and this relationship is likely to evolve in a changing climate (Holland and Stroeve 2011; DeRepentigny et al. 2016).

Motivated by this, we consider a region S, which we term the September-ice zone. We define S as the union of two regions: 1) the grid points covered by September sea ice (SIC $\geq 15\%$) in the model climatology and 2) the grid points with SIC standard deviation greater than 15%. This region, shown in Fig. 1a, is computed using the FLOR control run, and represents the region in which September sea ice is typically present. The area covered by the September-ice zone is $7.3 \times 10^{12}\,\text{m}^2$, a value similar to the observed SIE at the beginning of the satellite record.

b. The impact of earlier SIT on September SIC

As a motivation for our study of Arctic sea ice volume, we investigate the relationship between September SIC anomalies and earlier SIT anomalies, asking, what can earlier SIT tell us about September SIC? In Fig. 1b we show gridpoint correlation values between September SIC and May SIT in the FLOR control run. We choose to show May SIT correlations, as this is a forecast initialization month of practical interest to stakeholders. The largest correlations form an annulus of positive values, which surround the perennial sea ice located north of Greenland and the Canadian Archipelago. This annulus corresponds to the dominant region of September SIC variability and represents the spatial regions that could potentially benefit from an accurate initialization of May SIT in a seasonal forecast system. Note that the largest correlation in this figure is roughly 0.6, indicating that, on a gridpoint basis, May SIT explains less than 40% of September SIC variance. This will impose a practical upper limit on the regional forecast skill improvements achievable via improved SIT initialization.

However, given the spatial autocorrelation and consistently positive sign of the gridpoint correlation map, it is likely that an area-integrated metric will yield a stronger relationship between September SIC

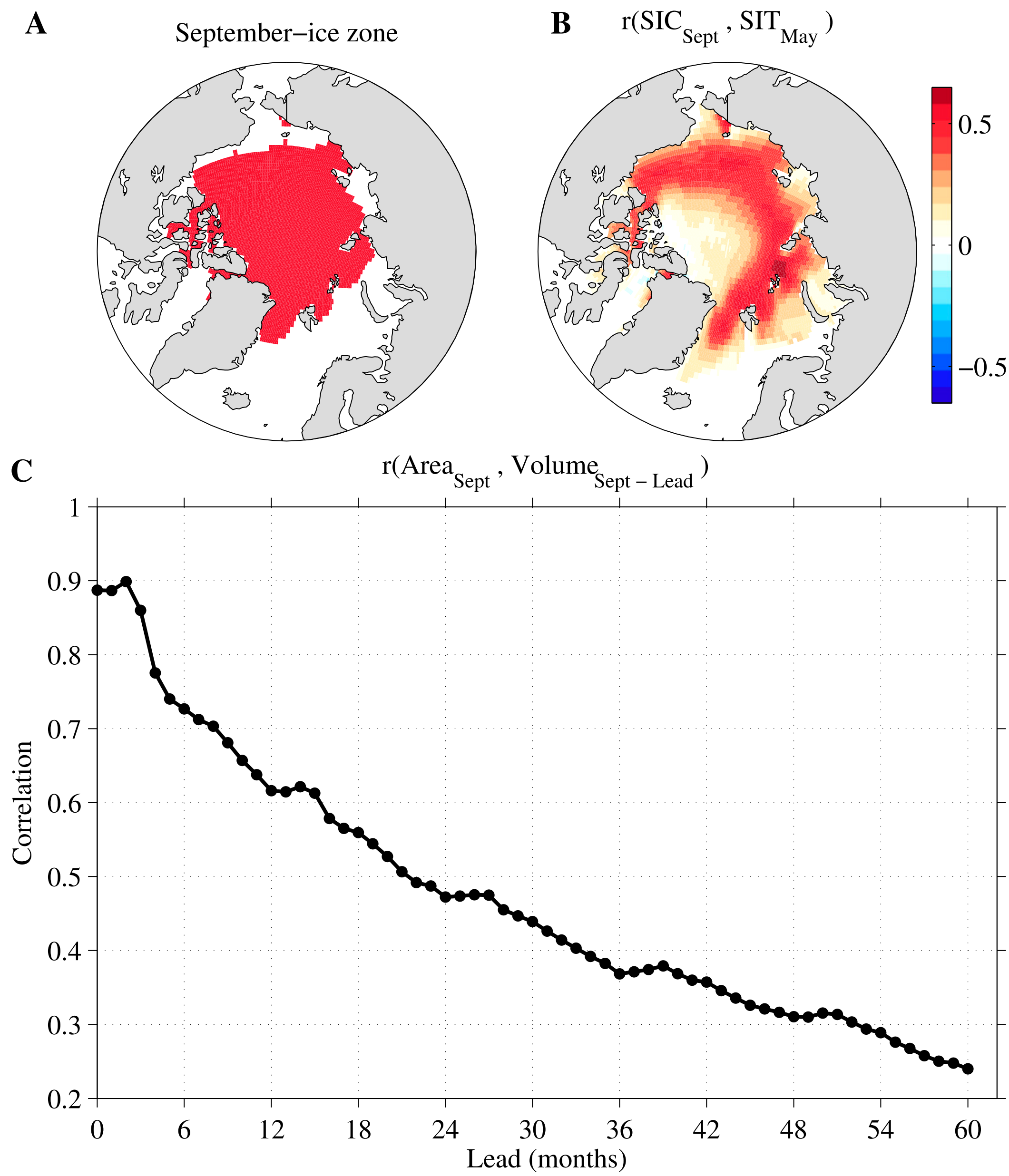

FIG. 1. Relation between September SIC and earlier SIT. (a) The September-ice zone, plotted in red. (b) Gridpoint correlation of May SIT and September SIC in the FLOR control run. (c) Lagged correlation between September sea ice area and earlier sea ice volume in the FLOR control run. The volume is computed over the September-ice zone.

and earlier SIT. In Fig. 1c, we show correlations between September sea ice area and earlier sea ice volume. The sea ice volume is computed over the September-ice zone, as this is the region where volume has the potential to impact September SIC. There is a strong positive correlation between September sea ice area and earlier sea ice volume, which decays with lead time. The correlation values are greater than 0.5 for leads up to 20 months, indicating a potential for SIT initialization to significantly improve seasonal forecast skill of September SIE. Interestingly, the lead-2-month correlations (September area with July volume) are slightly higher than the lead-0-month correlations (September area with September volume). The correlation curve also changes shape in July of years 1, 2, 3, and 4 (leads of 14, 26, 38, and 50 months), although the effect is smaller. This feature is related to a summer enhancement of sea ice volume anomalies, which is discussed in detail ahead. There is also a notable drop in correlation between lead 3 and lead 4 months (September area with June and May volume, respectively) and slower rates of decrease at lead times of 5–8 months. This feature may be related to the May predictability barrier identified in earlier work (Day et al. 2014b), in which perfect model forecasts of September SIE initialized in winter months have similar skill to those initialized in May. This indicates that observationally based SIT initialization in January–April could provide similar skill improvements to May initialization, a month where high-quality satellite SIT observations are not currently available.

c. *Volume anomaly time series*

The primary focus of this study is the temporal evolution of sea ice volume anomalies in the September-ice zone. We begin by computing a September-ice zone volume time series $V(t)$ defined as follows:

$$V(t) = \frac{1}{\rho_i}\int_S m(\mathbf{x}, t)\, dS, \tag{3}$$

where $\mathbf{x}$ is the latitude–longitude position, t is the time, $m(\mathbf{x}, t)$ is the mass of sea ice and snow per unit area, ρ_i is the density of sea ice in the model (905 kg m^{-3}), and S is the September-ice zone as defined above. The mass variable m output by SIS1 combines sea ice and snow mass. The contribution of snow mass to m is modest, ranging from roughly 5% in winter and spring to less than 1% over the summer. We also computed a September volume time series as $V(t) = \int_S c(\mathbf{x}, t)H(\mathbf{x}, t)\, dS$, where $c(\mathbf{x}, t)$ is the SIC and $H(\mathbf{x}, t)$ is the SIT in the ice-covered portion of the grid cell. This produces a similar time series to above, yielding the same qualitative conclusions that will be presented ahead in this study. We opt to define the volume time series in terms of ice mass, since the monthly mean volume is not necessarily the product of monthly mean SIC and monthly mean SIT. We next compute a monthly volume climatology $\overline{V}(t)$ by computing monthly means of $V(t)$. Subtracting the monthly climatology from $V(t)$, we obtain the September-ice zone volume anomaly time series $V'(t)$

$$V'(t) = V(t) - \overline{V}(t). \tag{4}$$

Note that by definition, $\overline{V'(t)} = 0$. Time series for $V(t)$ and $V'(t)$ computed using the FLOR control run are shown in Figs. 2a and 2b, respectively. The $V(t)$ time series has a clear seasonal cycle and also displays substantial variability on interannual-to-decadal time scales. This low-frequency variability is clearly visible in the $V'(t)$ time series and is possibly associated with low-frequency variations in oceanic heat transport into the Arctic Ocean (Zhang 2015).

We use the volume anomaly time series $V'(t)$ to study the evolution of volume anomalies in the September-ice zone. We identify high- and low-volume states by finding all times in which the volume anomaly exceeds a threshold of plus or minus 1.5 standard deviations ($\pm 1.5\sigma$; 1.4×10^{12} m^3), respectively. These thresholds are plotted as horizontal lines in Fig. 2b. Figure 2c shows the number of high- and low-volume "events" in the 700-yr time series, for each month of the year. We observe a clear seasonality in the event count, with more high- and low-volume states occurring over the summer months. Note that the September-ice zone is SIC anomaly free in winter, meaning that winter volume anomalies are driven solely by SIT, whereas SIC and SIT both contribute to the summer volume anomalies. To quantify the influence of SIC anomalies, we decompose the volume anomalies as $V' = \int_S (c'\overline{H} + \overline{c}H' + c'H')\, dS$. Computing this decomposition for high- and low-volume states, we find that the $\overline{c}H'$ term is dominant in all months, indicating that SIT anomalies are the primary contributor to ice-volume anomalies in the September-ice zone. Over the months of July–October, the $c'\overline{H}$ and $c'H'$ terms make notable contributions to V', with their sum ranging from 8% to 22% of the volume anomaly. Of particular interest in this study is the rapid increase of high- and low-volume events between May and July. This increase is due to enhancement of volume anomalies in the September-ice zone over these months. We describe this volume enhancement phenomenon in the following subsection.

d. *Summer volume anomaly enhancement*

The potential ability of improved winter and spring SIT initialization to influence September SIE predictions depends on how these SIT anomalies evolve between the initialization month and September. For instance, at some time scale, the model will relax to its free-running climatology, at which point the influence of SIT initialization will be lost. Here, we use the FLOR control integration to study the conditional evolution of volume anomalies in high- and low-volume states, for each month of the year. In Fig. 3, we plot high- and low-volume states for initial month January. We show the evolution of the volume anomaly time series for the two years following the initial January. Each black curve represents an individual high- or low-volume January, and the red curve is the conditional mean computed over all high- and low-volume Januaries.

The conditional mean curves display an unexpected feature: in addition to a general decay in time, the volume anomalies experience an enhancement over the summer months. This summer enhancement initiates in May and

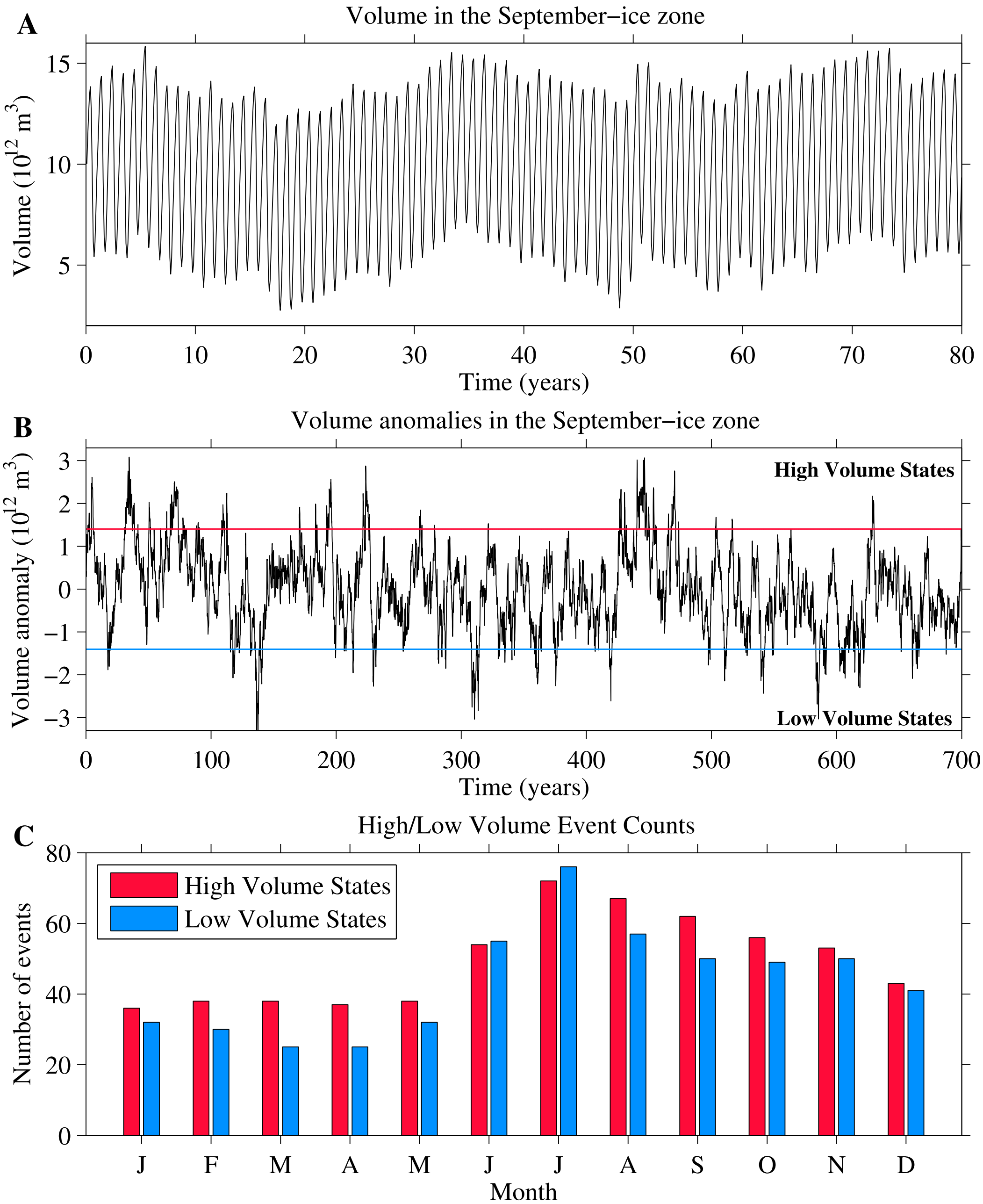

FIG. 2. (a) Time series of sea ice volume in the September-ice zone (80 yr shown here). (b) Sea ice volume anomaly time series in the September-ice zone. The red and blue lines represent $\pm 1.5\sigma$, respectively, the cutoffs used to define high- and low-volume states. (c) The number of high- and low-volume events over the 700-yr time series, in each month of the year. Note that there are more extreme volume events in summer months. On average, high-volume states have a slightly higher probability of occurrence than low-volume states (7.1% vs 6.2%).

reaches a maximum value in July, which is larger than the initial anomaly. After July, the volume anomalies begin to decay again, yet the August and September values remain comparable in magnitude to the initial January anomaly, owing to the summer enhancement. The volume anomalies decay through the ice-growth season and winter months, until May of the second year, when they display a second summer volume enhancement. The volume enhancement in year 2 is sufficiently large that the July anomaly in year 2 is of comparable size (in high-volume states; smaller in low-volume states) to the initial January anomaly from 18 months prior.

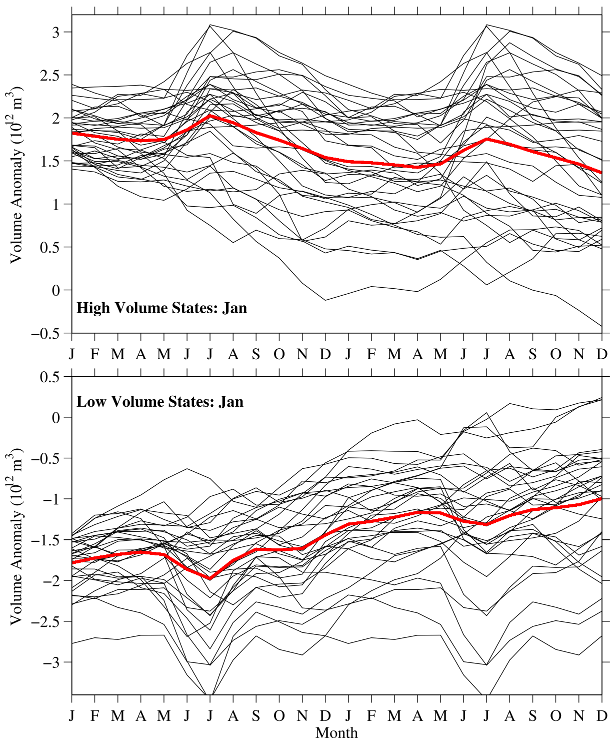

FIG. 3. Temporal evolution of September-ice zone volume anomalies, in (a) high- and (b) low-volume states. Each black curve represents two years of evolution of an individual high- and low-volume January. The red curves are the conditional mean over all high- and low-volume Januaries.

The evolution of volume anomalies is relatively symmetric in high- and low-volume states, with volume anomalies peaking in July in both year 1 and year 2. One notable difference is that the negative anomalies decay at a slightly faster rate than the positive anomalies. This asymmetry in decay rate is likely due to an asymmetry in the negative feedback between ice growth and ice thickness, as this feedback is particularly strong when the ice thins to values near zero.

It is important to note that the summer volume enhancement is a statistical feature of the volume evolution and there is a significant amount of internal variability to this phenomenon. In particular, any given year in Fig. 3 may evolve quite differently than the conditional mean. This is analogous to comparing a single ensemble member of an initialized forecast with the ensemble mean forecast. We will return to this concept in section 5, when we examine the summer volume enhancement phenomenon using an initialized forecast ensemble.

Next, we ask, is the timing of volume enhancement a function of the initial month? To investigate this, we compute conditional means for high- and low-volume states for each initial month of the year. The temporal evolution of these conditional means is plotted in Fig. 4. We observe a robust volume enhancement that peaks in July across all initial months and for high- and low-volume states. The temporal evolution is very similar for different initial months, which suggests that the mechanism for this summer volume enhancement is closely tied to the seasonal cycle, rather than being initial-month dependent. In this regard, this phenomenon is distinctly different from sea ice reemergence (Blanchard-Wrigglesworth et al. 2011a), in which the month of reemergence of SIC anomalies depends strongly on the initial month.

Figure 4 strongly suggests a positive feedback mechanism for this summer volume enhancement, as positive anomalies become more positive and negative anomalies become more negative. To further investigate the state dependency of volume enhancement, we compute conditional means over a continuous range of volume anomaly states. Specifically, we divide the volume anomalies into nine bins centered symmetrically around zero. The bin limits (in units of 10^{12} m^3) are $-\infty$, -1.5, -1, -0.5, -0.2, 0.2, 0.5, 1, 1.5, and ∞. We place each January from the 700-yr simulation into one of these bins and compute conditional means within each bin (plotted in Fig. 5a). We find that the summer volume anomaly enhancement occurs in all bins other than the zero-centered bin, indicating that this phenomenon is present in nearly all volume states. Moreover, we find that the strength of this enhancement scales smoothly with the size of the initial volume anomaly. In Fig. 5b, we plot the summer volume anomaly change ΔV (defined as $\Delta V = V'_{\text{July}} - V'_{\text{May}}$) versus the January volume anomaly V'_{Jan}. This shows a clear positive relationship between the size of January anomalies and the amount of summer volume enhancement. This relationship is opposite of what one would expect from a red-noise null hypothesis: If $V'(t)$ behaved as a red noise process, for $V'_{\text{Jan}} > 0$, one would expect $\Delta V < 0$, and for $V'_{\text{Jan}} < 0$, one would expect $\Delta V > 0$. Indeed, this is what we find if ΔV is computed using month pairs outside of the summer (e.g., December and October). This clear deviation from red-noise behavior over the summer months indicates the presence of positive feedbacks in the Arctic system.

e. *Spatial composites in high- and low-volume states*

We have documented a summer enhancement of sea ice volume anomalies in the September-ice zone. Next, we consider the spatial patterns of this volume enhancement. In Fig. 6, we plot monthly composite maps of the SIT anomaly field, computed over all years with high-volume Januaries. The composite maps are relatively insensitive to the choice of initial month and are qualitatively similar, with opposite sign, for low-volume states. The high-volume states are characterized by positive SIT anomalies that extend

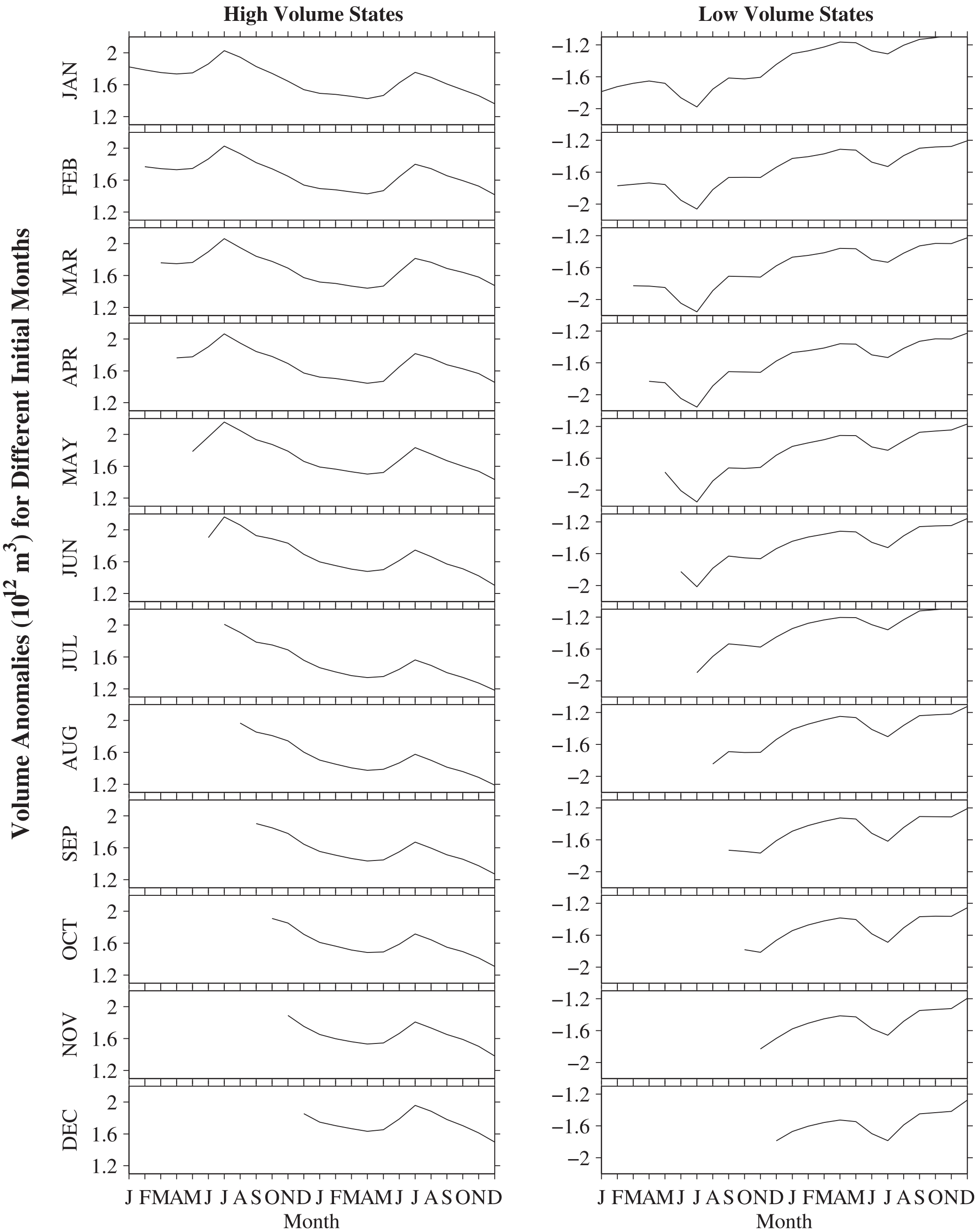

FIG. 4. Evolution of volume anomalies in the September-ice zone for different initial months and (left) high- and (right) low-volume states. Each of these curves is a conditional mean, computed over all high- or low-volume states for the given initial month. Note that the summer enhancement consistently peaks in July for all initial months.

throughout the September-ice zone. The monthly evolution of these SIT anomalies exhibits a similar summer enhancement to the volume anomaly time series, with enhanced anomalies beginning in June and extending into July, August, and September. This summer SIT enhancement encompasses a broad spatial scale, covering most of the September-ice zone, indicating that the summer enhancement is a spatially distributed effect. After September, the SIT anomalies begin to thin to smaller values, driven by negative feedbacks from sensible and latent heat fluxes (see section 4, ahead).

In Fig. 6, we also plot corresponding monthly composite maps for the SIC anomaly field. The winter and spring months display very little SIC anomaly, as the

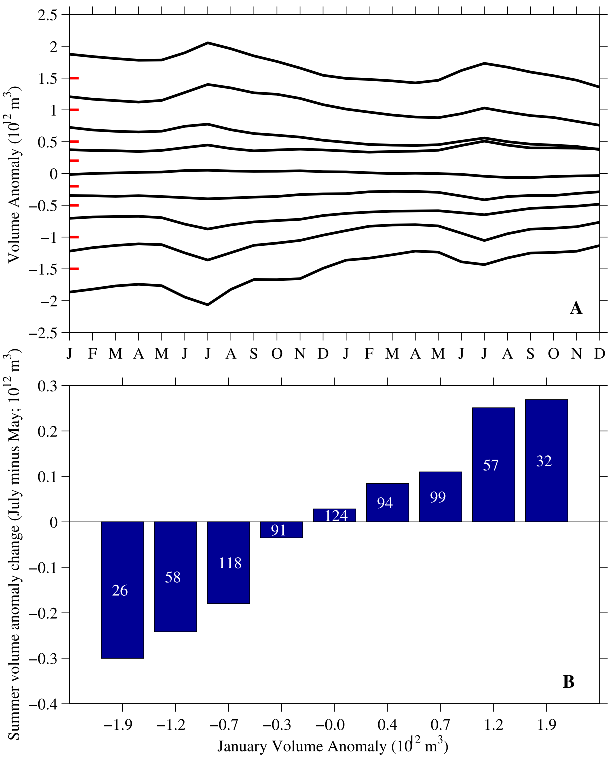

FIG. 5. (a) Volume anomaly evolution for different January volume states. Each January is placed into a volume bin (bin limits shown in red on the y axis), and conditional means within each bin are computed. (b) Summer volume anomaly enhancement (July volume anomaly minus May volume anomaly) vs January volume anomaly. The white numbers indicate the number of Januaries that fall within each volume bin. The x-axis values are the mean January volume anomaly within each bin [the y intercepts in (a)].

September-ice zone is fully covered by sea ice in these months. In the summer and early fall, particularly July–October, we observe an annulus of positive SIC anomalies located near the edge of the September-ice zone. This shows that high-volume Januaries tend to produce summers with more extensive sea ice. Also, it is important to note that the month of June is nearly SIC-anomaly free. The summer volume enhancement, however, has already begun in June (see Fig. 3), which suggests that the volume enhancement is not being driven exclusively by SIC anomalies. We examine the physical mechanisms that drive the summer volume enhancement in the following section.

4. Mechanisms for volume enhancement

a. Surface energy budget

To understand the mechanisms responsible for the observed summer volume enhancement, we begin by considering the surface energy budget over the Arctic Ocean. The net surface heat flux (at the atmosphere–ice and atmosphere–ocean interfaces) F_{sfc} is given by

$$F_{\mathrm{sfc}} = \mathrm{SW} + \mathrm{LW} + \mathrm{SH} + \mathrm{LH}, \quad (5)$$

where SW is the absorbed shortwave radiation flux (shortwave down minus shortwave up), LW is the absorbed longwave radiation flux (longwave down minus longwave up), SH is the sensible heat flux, and LH is the latent heat flux. (A schematic, showing the various terms in the surface energy budget, is shown in Fig. 11a.) Note that each term in this equation is defined as positive downward. Therefore, positive terms contribute to melting ice and negative terms contribute to freezing ice. To study the mechanisms for summer volume enhancement, we consider the conditional evolution of these surface heat flux terms in high- and low-volume states.

For each variable, we compute a spatial-mean time series, where the area integration is performed over the September-ice zone. Subtracting a monthly climatology, we obtain an anomaly time series. Next, we form conditional means from these anomaly time series, computed over all high- and low-volume Januaries. In Fig. 7, we plot the 2-yr evolution of these conditional means for a number of different variables. The SIT anomaly evolution displays a similar summer enhancement to the volume anomaly time series, with thick anomalies becoming thicker and thin anomalies becoming thinner over the summer months.

The dominant contribution to surface energy budget anomalies between May and August comes from SW. In high-volume states, there are negative SW anomalies in May through September, with a spatial-mean value of roughly $-2\,\mathrm{W\,m^{-2}}$. The magnitude of the summer SW anomalies substantially exceeds the other terms of the surface energy budget and is also larger than their sum (LW + SH + LH; see Fig. S1 of the supplementary material for the evolution of each term in the surface energy budget). We observe a similar behavior in low-volume states, with positive SW anomalies spanning the months of May through August. Are these SW anomalies large enough to explain the observed SIT anomaly enhancement?

To check this, we compute a quantity E, defined as the time-integrated SW anomaly over the months in which the SIT anomalies are enhanced (May through July). If all of the anomalous shortwave energy is used to melt or freeze ice, then $E = \rho_i L \Delta z$, where $\rho_i = 905\,\mathrm{kg\,m^{-3}}$ is the density of sea ice in the model, $L = 3.34 \times 10^5\,\mathrm{J\,kg^{-1}}$ is the latent heat of fusion of ice, and Δz is the thickness change in meters. Computing Δz for high- and low-volume states, we find $\Delta z = 0.05$ and $-0.09\,\mathrm{m}$, respectively. Performing a similar computation based on

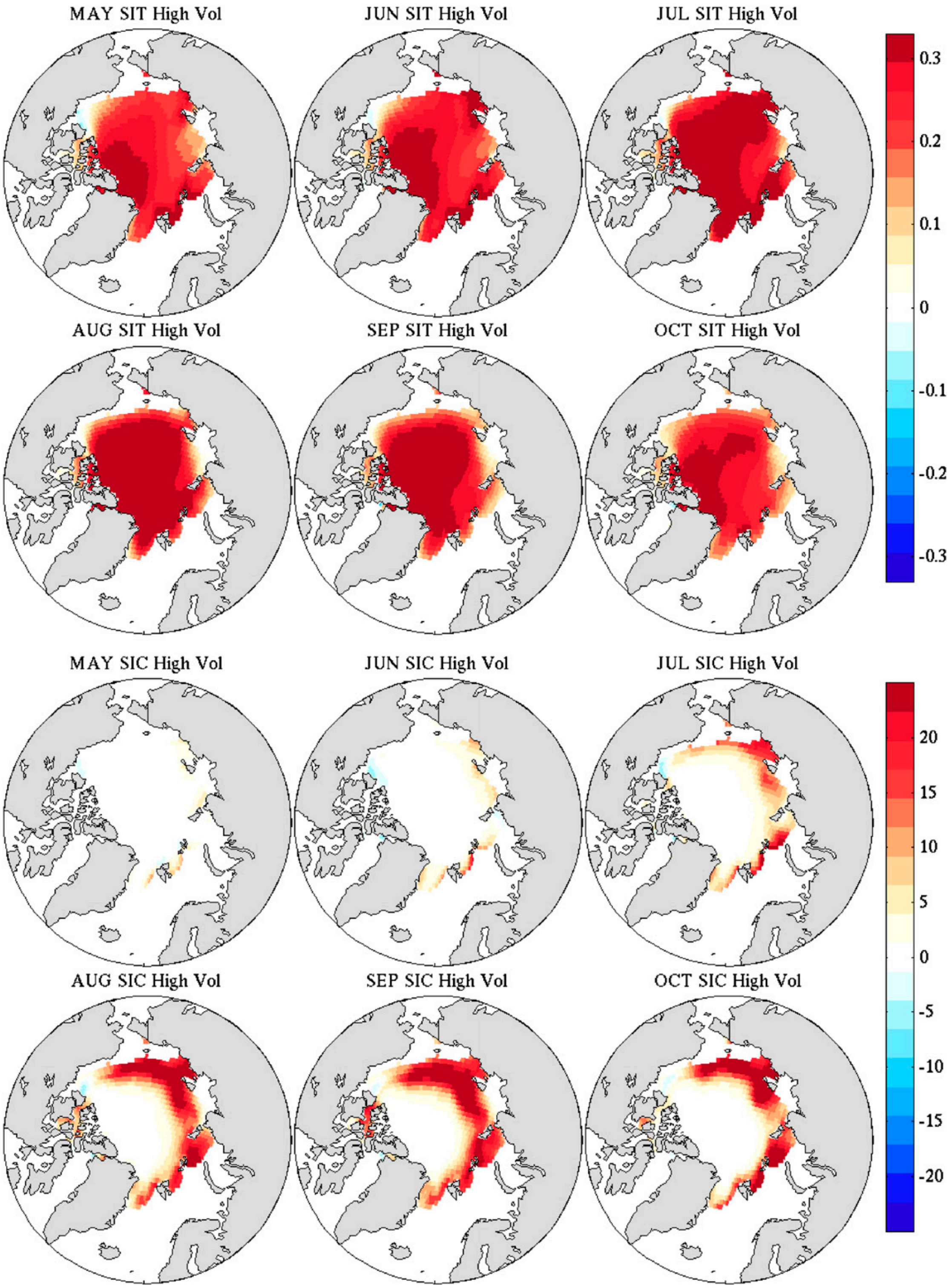

FIG. 6. High-volume composites for (top) SIT (m) and (bottom) SIC (%) anomalies computed over all years with high-volume Januaries. Only anomalies in the September-ice zone are plotted.

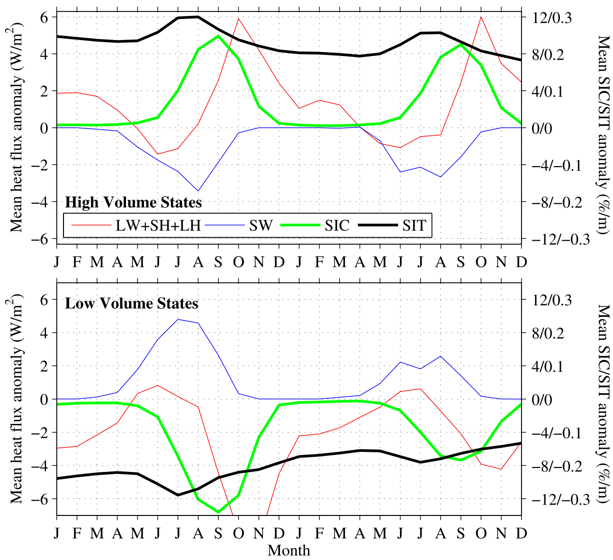

FIG. 7. The surface heat budget over the September-ice zone in (top) high- and (bottom) low-volume states. Shown are the conditional evolution of net SW anomalies, the sum of LW, SH, and LH anomalies, SIC anomalies, and SIT anomalies. All terms are spatial averages computed over the September-ice zone. Positive heat fluxes contribute to melting ice and negative fluxes contribute to freezing ice.

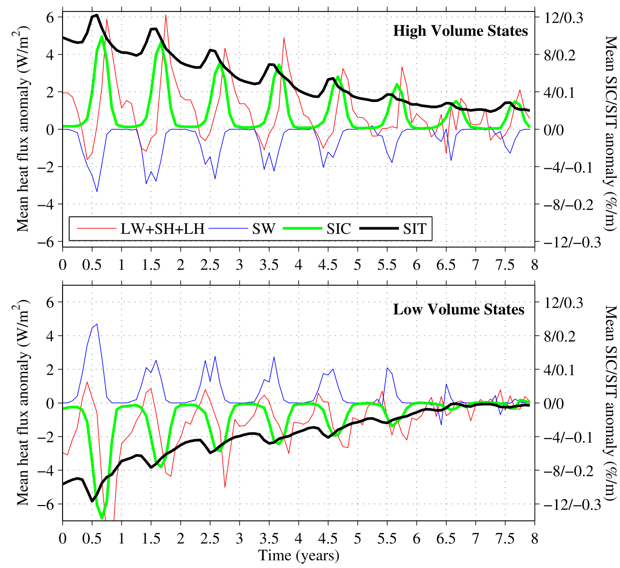

FIG. 8. The surface heat budget over the September-ice zone in (top) high- and (bottom) low-volume states plotted for 8 yr of time evolution. Positive heat fluxes contribute to melting ice and negative fluxes contribute to freezing ice.

LW + SH + LH, we find that these heat fluxes correspond to thickness changes of $\Delta z = 0.02$ and -0.01 m for high- and low-volume states, respectively. These changes are small compared with the SW estimates, indicating that the summer thickness changes are indeed dominated by SW anomalies. Summing these two contributions, we recover total thickness changes of $\Delta z = 0.07$ and -0.10 m in high- and low-volume states, respectively. The actual observed thickness changes are 0.07 and -0.07 m for high- and low-volume states, respectively, which agree quite well with the above estimates. The discrepancy in the low-volume estimate is likely because some of the SW signal is absorbed into the ocean and is not directly used to melt or freeze ice. This issue does not arise in high-volume states because the September-ice zone is close to being fully ice covered in these states.

Following the summer SIT enhancement, the SW anomalies become weaker, reaching a near-zero value in October. The sensible and latent heat flux terms become large in September through November, arising as a lagged response to SIC anomalies, which peak in September (see Fig. S1 of the supplementary material). Note that the LW anomalies are weak during these months, therefore the LW + SH + LH term is dominated by SH + LH. In high-volume states, positive September SIC anomalies provide a barrier between the atmosphere and ocean, reducing surface evaporation and also reducing the sensible heat flux from the ocean to atmosphere. These effects produce positive anomalies in latent and sensible heat flux (note that we are using the convention of positive downward). There is also a weaker LW signal (see Fig. S1), with positive LW anomalies from December–April and negative LW anomalies from May–August. The same behavior, with opposite sign, occurs in low-volume states.

Year 2 displays similar relationships, with smaller amplitude, between SIT, SIC, and the surface heat budget terms. In Fig. 8, we consider the longer-timescale evolution of these fields, in high- and low-volume states. We find a consistently recurring summer SIT enhancement, with a discernible signal for five years beyond the initial thickness anomaly. There are also consistently recurring surface energy relationships in each year, characterized by synchronous SW anomalies and SIT enhancement, followed by SIC anomalies, and then followed by latent and sensible heat flux anomalies. We have shown earlier that the size of the summer enhancement is proportional to the SIT anomaly magnitude (Fig. 5). Here, we additionally find that the magnitudes of the SW, SIC, and LW + SH + LH anomalies scale with the magnitude of the SIT anomaly. The fact that the SW anomaly scales with the SIT anomaly further supports the hypothesis that the summer enhancement is SW driven. In both high- and low-volume states, the anomalies decay within a roughly exponential envelope, with e-folding time scales of 4.6 and 3.1 yr, respectively (estimated based on exponential fits to the SIT anomaly curves). Other GCMs will likely

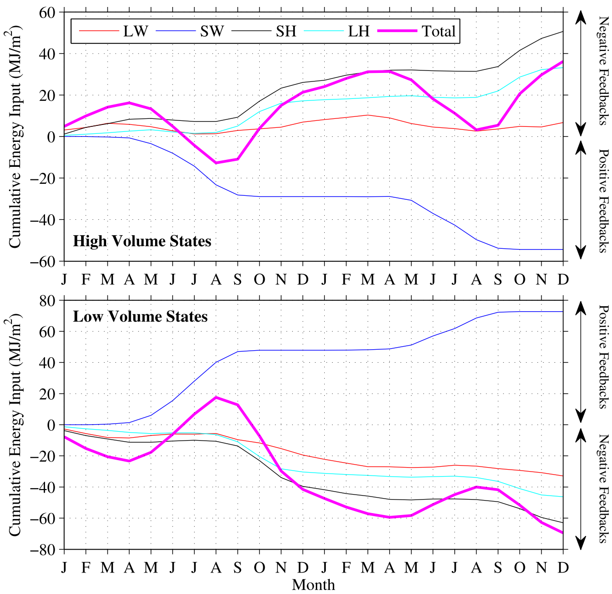

FIG. 9. The cumulative anomalous energy input from each term in the surface energy budget in (top) high- and (bottom) low-volume states. The magenta line shows the cumulative energy input from the sum of the four terms. Positive energy input contributes to melting ice and negative energy input contributes to freezing ice.

have different anomaly decay characteristics and possibly a different representation of summer volume enhancement. Future work is required to explore these directions.

Next, in Fig. 9, we consider the cumulative anomalous energy input from each term in the surface energy budget (i.e., the running time integral of the fluxes in Fig. S1). In high-volume states, the SW term provides a net negative energy input, a positive feedback, whereas the other terms provide negative feedbacks via their positive energy input. The sum total of the four terms exhibits a positive secular trend, indicating that the fluxes generally act to relax the volume anomaly toward zero. Each summer this secular trend is temporarily reversed as a result of the positive feedback contribution from the SW term. The largest negative feedbacks come from sensible and latent heat fluxes, with the sensible heat contribution being the slightly larger of the two. The negative feedbacks from these terms are strongest over the months of September–December, likely associated with the SIC anomalies present in these months. In low-volume states, similar relationships hold, with SW providing the positive feedback and LH, SH, and LW providing negative feedbacks.

b. *Volume-driven changes in surface albedo*

We have shown that summer sea ice volume changes are driven primarily by anomalies in shortwave radiation. Next, we argue that the summer shortwave anomalies result from a positive feedback between the volume state and surface albedo. The volume state can potentially influence surface albedo in four distinct ways: 1) changes in SIC (the ocean has lower albedo than sea ice), 2) changes in SIT (thin ice has lower albedo than thick ice), 3) changes in snow cover on sea ice (bare sea ice has a lower albedo than snow-covered sea ice), and 4) changes in surface melt (wet sea ice and snow have lower albedos than their dry counterparts). We next consider the individual contributions to surface albedo from each of these four factors. In Figs. 10a,b, we plot the conditional anomaly evolution of variables relevant to surface albedo. In Figs. 10c,d, we place these contributions on common axes, providing estimates of the surface albedo changes that result from these anomalies. For simplicity, the analysis below is primarily focused on high-volume states, but the same arguments apply symmetrically to low-volume states.

First, we consider the effect of SIC on surface albedo. We find that high-volume states have positive SIC anomalies over May–October (Fig. 10a), which produce positive albedo anomalies and negative SW anomalies over these months. To quantify this albedo impact, we compute an albedo response function, defined as the surface albedo change resulting from a +1% change in SIC. This albedo response function is computed from the model's albedo difference between sea ice and ocean albedo, which varies seasonally. For example, the value of the response function in May is +0.69% compared with +0.45% in August, since snow-covered May ice has a substantially higher albedo than the surface-melted August ice (see Fig. S2 of the supplementary material). This monthly dependence places additional weight on SIC anomalies in the early melt season, implying that the relatively modest SIC anomalies of May and June can have an important impact on surface albedo. In Fig. 10c, we plot the estimated surface albedo anomaly resulting from SIC, obtained by multiplying the SIC anomaly curve in Fig. 10a by the albedo response function. We find that SIC is the dominant contributor to surface albedo anomalies in July–September. In May and June, the SIC-based anomalies are comparable in magnitude to the anomalies that result from snow area and surface skin temperature. Note that the SW curve peaks earlier than the albedo maximum because SW = $(1 - \alpha)$swdn, where swdn is the downwelling shortwave radiation. SW peaks in August, between the swdn maximum at the summer solstice in late June and at the albedo anomaly maximum in September. Next, we perform a similar analysis for other variables that influence surface albedo: snow, thin ice concentration, and surface skin temperature.

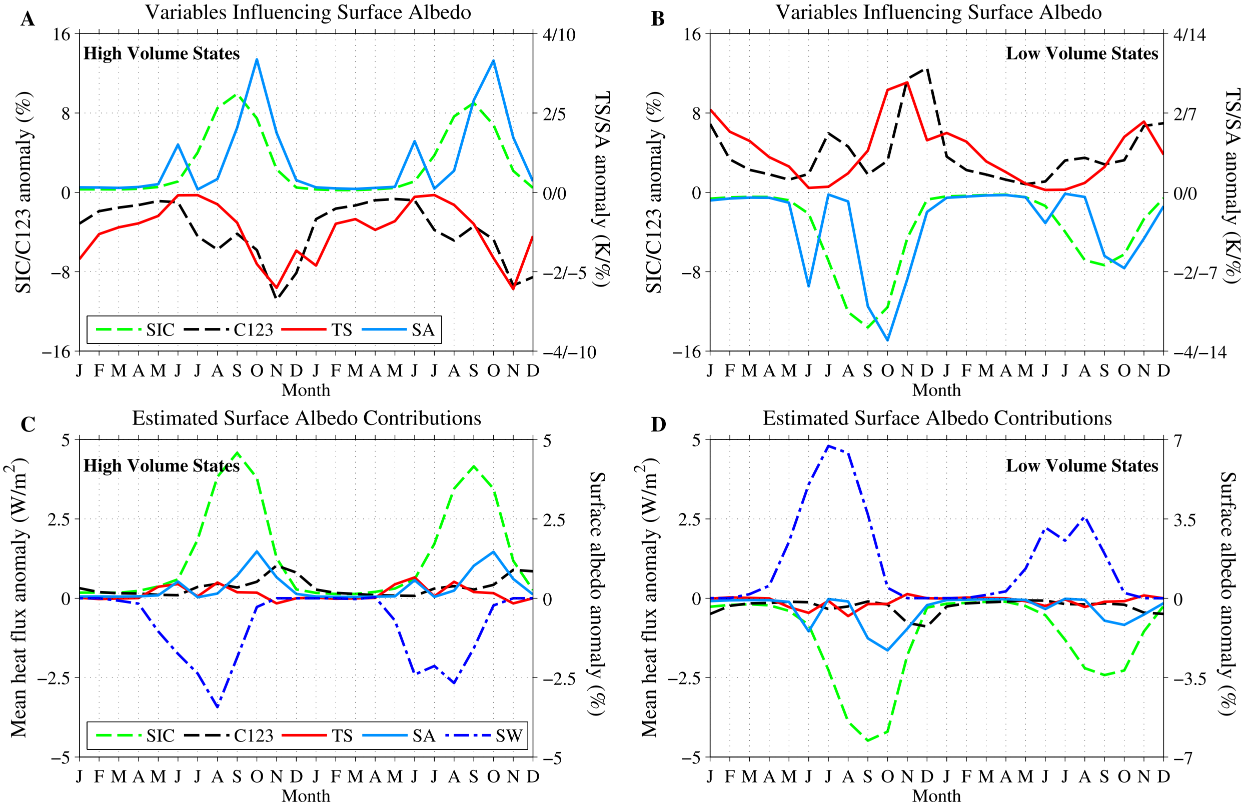

FIG. 10. Time evolution of variables influencing surface albedo in (a) high- and (b) low-volume states. Plotted are the conditional evolution of SIC, the concentration of ice in categories 1, 2, and 3 (C123), the surface skin temperature (TS), and the area of snow-covered ice (SA). The snow area is normalized by the area of the September-ice zone. Note that a different y scale is used for snow area anomalies in high- and low-volume states. (c),(d) Estimates of the surface albedo anomaly resulting from the anomalies shown in (a) and (b). The SW anomaly is what we seek to explain.

In this model, the September-ice zone is fully snow covered in May and completely snow free in July. June is the transition month in which the snow cover on sea ice melts. Given the albedo difference between snow and sea ice, the timing of this snowmelt has important implications for June surface albedo. We consider a snow-area variable, defined as the areal sum of all grid cells that have a snow thickness of at least 0.02 m. We find that June has positive snow-area anomalies in high-volume states, which creates a positive albedo anomaly. There are also large snow-area anomalies in the fall months. These anomalies are the result of SIC anomalies: the positive SIC anomaly in high-volume states results in a larger areal platform to collect snowfall in the fall months. Analogous to SIC, we compute an albedo response function for snow area. For this function, we use the average value of the difference between snow and ice albedos quoted in section 2a, yielding a response function of +0.176% for every +1% snow-area anomaly. Snow area contributes a positive albedo anomaly in June, which is consistent with the negative SW anomaly in this month. While the June snow-area anomaly appears dominant in Fig. 10a, its corresponding albedo anomaly (Fig. 10c) is of comparable magnitude to that resulting from SIC.

In the sea ice model, ice that is thinner than 0.5 m has a reduced albedo, as shown in Eq. (2). This albedo reduction depends on the thicknesses h_i and concentrations c_i in each ice-thickness category. We do not have h_i values saved as output data for this model, but we do have c_i (note that SIC = $\sum_{i=1}^{5} c_i$). The thickness boundaries that define the five ice-thickness categories in the FLOR model are 0.1, 0.3, 0.7, and 1.1. Therefore, sea ice in categories 1, 2, and the first half of 3 has reduced albedo because of its thickness. We find that, in addition to positive SIC anomalies, high-volume states have negative ice concentration anomalies in categories 1–4 and positive anomalies in category 5 (not shown). In particular, the thin-ice categories (1–3) have negative concentration anomalies over the summer and fall months (see Fig. 10a). These anomalies are negligible in June but are notably negative in July through September and reach more negative values in October through December. We compute an albedo response function (see Fig. S2) for thin ice concentration using Eq. (2) and an assumption that the mean thickness of ice in categories 1–3 is 0.3 m. We find that thin-category ice creates a small positive albedo anomaly in July–September. This surface albedo anomaly is consistent with the negative SW anomaly observed over these months, but its magnitude is negligible compared to the influence of SIC.

Finally, we consider T_s, the surface skin temperature, which is determined from the surface energy balance and plays a role in the spring melt onset of sea ice. In Fig. 10a, we find that high-volume states have negative winter T_s anomalies, which are the result of colder ice temperatures in the thicker ice (not shown). The negative T_s anomalies persist into the spring months and begin to affect surface albedo in May via Eq. (1). Note that T_s does not influence albedo before May because the T_s values are sufficiently negative that Eq. (1) always uses the α_{dry} values. Anomalously cool surface temperatures in May delay the onset of surface melt, resulting in a positive surface albedo anomaly and a negative anomaly in SW. Unlike the other variables considered above, it is not straightforward to convert a given T_s anomaly into a surface albedo anomaly since the effect of T_s on surface albedo occurs indirectly via Eq. (1). To compute an albedo response function for T_s, we use a multiple linear regression in which surface albedo is predicted using SIC, snow area, thin ice concentration, and T_s as predictor variables. This multiple linear regression is computed on a monthly basis and the regression coefficient for T_s provides the surface albedo response owing to a +1-K anomaly in T_s. We find that T_s contributes surface albedo anomalies in May and June that are comparable in magnitude to the SIC contribution. The influence of T_s is relatively small over July–September, when the albedo anomaly is dominated by SIC.

A schematic summary of the volume enhancement mechanism is shown in Fig. 11b. The summer volume enhancement is driven by a positive feedback between surface albedo and the sea ice state. In May and June, the feedback is dominated by changes in SIC, the melt-onset date, and snow area on sea ice. In July and August, the feedback is dominated by changes in SIC alone. In years 2 through 5 of Fig. 8 there are two distinct peaks in SW, corresponding to June and August anomalies, respectively. This distinct separation is consistent with the fact that different mechanisms drive the SW anomalies in June versus August. It is important to note that this mechanism is based on a set of nonlinear feedbacks, and therefore there are limitations to the linear separation of albedo factors presented in Figs. 10c,d. In particular, the present analysis cannot identify a causal chain of events that initiate the ice–albedo feedback. Further model experiments would be required to quantify the relative importance of SIC and surface ice properties in initiating this feedback.

An implicit assumption in the above mechanism is that the SW anomalies are driven by surface albedo changes, rather than changes in swdn. Since SW = $(1 - \alpha)$swdn, the negative SW anomalies in high-volume states could result from either a negative swdn anomaly or a positive albedo anomaly. To check this, we compute swdn anomalies in high- and low-volume states. We find positive swdn anomalies in high-volume states and negative swdn anomalies in low-volume states; the opposite of the anomalies necessary to explain the observed SW anomalies. From this, we conclude that the SW anomalies are indeed surface-albedo driven.

c. Ice–ocean energy budget

The analysis to this point has focused on the surface energy balance (i.e., the energy balance at the atmosphere–ice and atmosphere–ocean interfaces). We next consider the energy balance at the ice–ocean interface, with the goal of diagnosing the primary driver of melt at this interface. In particular, there is a possibility that the observed volume changes are being driven by oceanic turbulent heat flux (TH). We let F_{ocean} be the net ice–ocean heat flux. This term has contributions from F_{sfc} via direct transmission into the ocean surface through sea ice leads or transmission through sufficiently thin sea ice and from TH via ocean mixing. The term F_{ocean} is saved as a model diagnostic, but the individual contributions from the transmitted surface heat flux and TH are not. Therefore, we estimate the transmitted heat flux from each term in the surface energy budget, as detailed in section a of the appendix. The computation of transmitted SW (SWT) uses Beer's law to estimate transmission through sea ice (see appendix; section 3.6.2 of Hunke et al. 2015). This estimate likely underestimates the magnitude of SWT due to the temporal resolution of the data; however, it does capture its temporal variability. We let $F_{\mathrm{sfc\text{-}t}}$ be the portion of the net surface heat flux that is directly transmitted into the ocean surface.

We find that the total May–July F_{ocean} and total May–July $F_{\mathrm{sfc\text{-}t}}$ are highly correlated (r = 0.93), indicating that a large fraction of F_{ocean} variance (87%) is captured by $F_{\mathrm{sfc\text{-}t}}$. This substantial covariance highlights an important point: surface heat flux anomalies are coupled to the ocean and can ultimately contribute to melting sea ice at the ice–ocean interface. Indeed, we find that the F_{ocean} anomalies in high- and low-volume states correspond to ice-thickness changes of $\Delta z = 0.04$

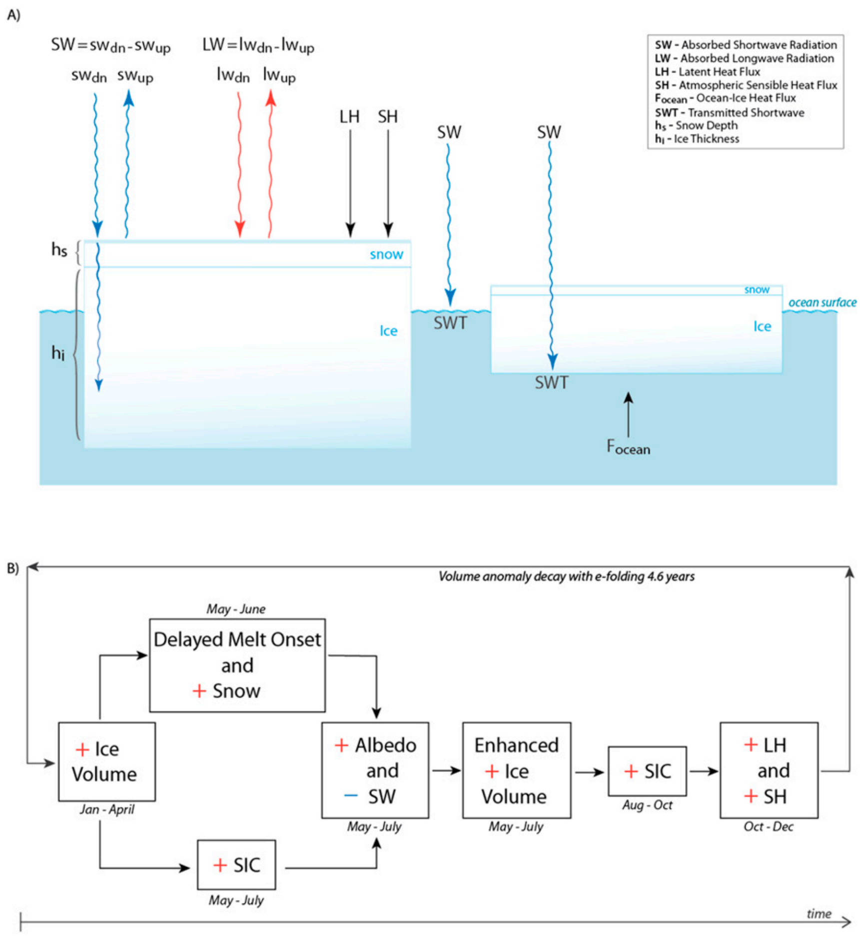

FIG. 11. (a) Schematic of the heat fluxes in the surface energy budget. (b) Summary of the mechanism for summer enhancement of sea ice volume anomalies.

and -0.05 m, respectively. These represent a substantial fraction of the ice-thickness changes from volume enhancement of $\Delta z = 0.07$ and -0.07 m reported in section 4a. The strong covariance of the transmitted surface heat flux and the ice–ocean heat flux indicates that TH does not play a leading role in driving the summer volume anomaly enhancement. This is consistent with the expectation that vertical mixing is weak in the strongly stratified central Arctic Ocean. Also, one would expect the reduced (additional) melt in high- (low-) volume states to decrease (increase) surface stratification, thereby increasing (decreasing) vertical mixing and providing a negative feedback for the volume anomaly. Therefore, the vertical mixing contribution has the incorrect sign to explain the observed volume anomaly enhancement.

Of the four terms in the surface energy budget, SWT is the dominant contributor to $F_{\text{sfc-t}}$ (98% of the variance) over the volume enhancement months of May–July. This suggests that the ice–ocean heat flux in May–July is primarily shortwave driven. Note that while the SW anomaly occurs at the surface, it influences the sea ice in three distinct ways: 1) top melt at the ice–atmosphere interface; 2) warming of the interior ice via shortwave absorption, which influences both top and bottom melt by modifying conductive heat fluxes in the ice; and 3) bottom melt at the ice–ocean interface.

5. Implications for Arctic seasonal predictability

a. *Volume enhancement in an initialized forecast system*

Using a control run, we have demonstrated that volume anomalies in the September-ice zone are enhanced over the summer months. What are the implications for seasonal predictions made with initialized forecast ensembles? To examine this question, we compare the FLOR and $\text{FLOR}_{\text{SITpert}}$ prediction ensembles. These ensemble experiments use the same dynamical model and, besides

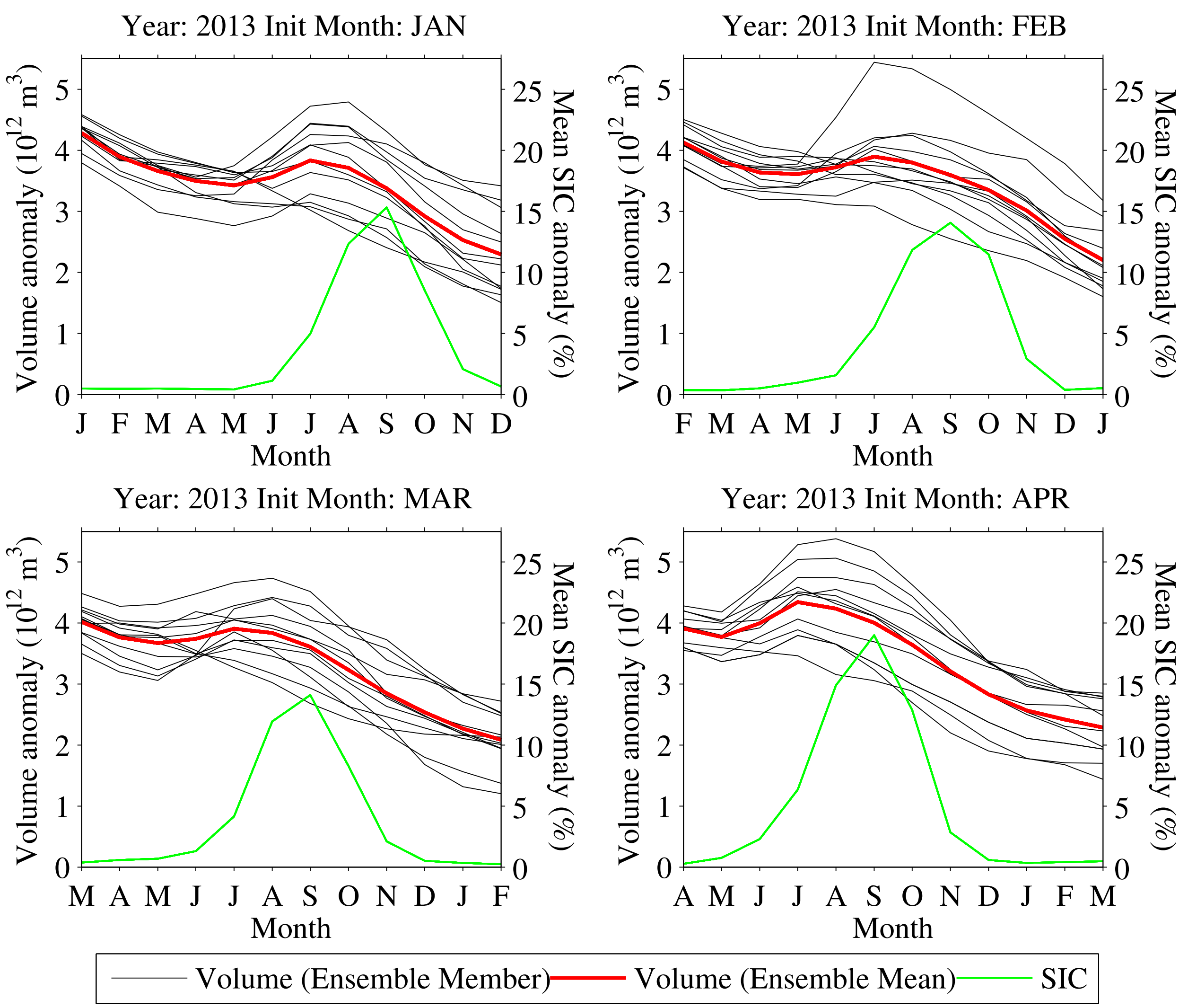

FIG. 12. Volume anomaly and SIC anomaly evolution for ensemble predictions initialized on 1 January, 1 February, 1 March, and 1 April 2013. Anomalies are defined as $\mathrm{FLOR}_{\mathrm{SITpert}}$ minus FLOR. Each black curve represents the volume anomaly of an individual ensemble member, and the red and green curves are ensemble means of the volume and SIC anomalies, respectively.

SIT, share identical initial conditions. The $\mathrm{FLOR}_{\mathrm{SITpert}}$ experiments are initialized with thicker SIT, as described in section 2b and section b of the appendix. We compare the FLOR and $\mathrm{FLOR}_{\mathrm{SITpert}}$ runs to study the system's memory of SIT initial conditions. Analogous to section 3, we study the evolution of sea ice volume anomalies in the September-ice zone. We define anomalies for each perturbed ensemble member as $\mathrm{FLOR}_{\mathrm{SITpert}} - \langle\mathrm{FLOR}\rangle$, where angle brackets indicate an ensemble mean.

In Fig. 12, we plot 12 months of volume anomaly evolution for forecasts initialized in January through April 2013. All forecasts are initialized on the first of the month and run with 12 ensemble members. We find significant persistence of the initial SIT anomalies, with 48 of 48 ensemble members displaying a positive volume anomaly 12 months after initialization. The mean *e*-folding time scale of these volume anomalies is 2.0 yr. This indicates that, in this forecast system, SIT initialization has the potential to impact forecast skill for lead times up to roughly 24 months. In addition to their volume memory, the ensemble means show a summer volume enhancement that closely resembles that of the control run. For each initialization month, the volume enhancement begins in May and peaks in July. As in the control run, the volume enhancement is a statistical feature, which is visible in the ensemble mean but not necessarily in every ensemble member. The mean volume enhancement (over all start dates) is 0.38×10^{12} m^3, which is roughly 30% larger than the largest volume enhancements shown in Fig. 5. The initial volume anomalies in the ensemble runs are significantly larger (4σ) than the typical anomalies in the control run, which is consistent with this increased enhancement. Figure 12 also shows the ensemble-mean evolution of spatial-mean SIC anomalies, which are defined analogously to the volume anomalies. For all initialization months, the SIC anomalies are positive over the summer months and peak in September. This SIC behavior is consistent with the findings from the control run and demonstrates a clear influence of SIT initialization on September SIE.

b. *Implications and discussion*

The ensemble prediction experiments show that SIT initial condition perturbations are persistent on seasonal time scales and, moreover, that these perturbations are enhanced over the summer months. This indicates a promising potential for improvements in winter and spring SIT initialization to impact and improve seasonal forecasts of September sea ice. Since the SIT enhancement occurs over the summer months, this phenomenon is particularly relevant for predictions of September sea ice. It is important to note that in the $\mathrm{FLOR_{SITpert}}$ experiments, only the SIT initialization was changed. This is distinct from the control run, in which SIT anomalies exist as part of a fully consistent ice–ocean–atmosphere–land state. The fact that a robust volume enhancement occurs with changes to solely SIT allows us to directly attribute volume enhancement to the thickness state.

The summer volume enhancement is driven by a state-dependent albedo feedback, which, in May and June, is controlled by SIC, surface melt onset, and snow cover. This suggests that an accurate representation of SIC and ice-surface conditions in May and June are crucial for accurately capturing volume, and hence SIC, evolution through the summer months. While satellite SIT observations are not currently available in May and June because of challenges associated with surface melt, SIC and melt pond data are available and may encode crucial information about the SIT state. This suggests a potential future initialization strategy, in which satellite SIC data are assimilated in all months and satellite SIT data are assimilated in the winter and early spring months (up to the end of April), after which satellite-derived melt pond data are assimilated for May and June. This strategy would allow thickness-related data to be assimilated well into the melt season, potentially improving September predictions. Indeed, recent work has shown that melt ponds are a source of predictability for September sea ice, although there is some disagreement regarding the lead times at which this predictability is realized (Schröder et al. 2014; Liu et al. 2015).

Another recent study shows that prediction ensembles initialized in May with realistic sea ice conditions show improved seasonal forecast skill compared to ensembles initialized with a sea ice climatology (Guemas et al. 2016). The initialized ensembles in Guemas et al. (2016) show a summer enhancement of SIE forecast skill, which resembles the volume enhancement signal in this study lagged by roughly one month. These results suggest that summer SIT anomaly enhancement increases the predictability of September SIE. Additional future work is required to understand the impact of summer volume enhancement on September SIE prediction skill.

6. Conclusions

Using a control integration and a suite of initialized forecast ensembles from a fully coupled global climate model (GCM), we have examined the temporal evolution of sea ice volume anomalies in the September-ice zone. The September-ice zone is the region where September sea ice is typically present and, therefore, the region where sea ice thickness (SIT) has greatest potential to influence September sea ice concentration (SIC). We have found that the control simulation has a strong correlation between September sea ice area and earlier sea ice volume in the September-ice zone. These correlation values are greater than 0.7 for leads of 0–8 months and remain above 0.5 up to a lead of 20 months. Interestingly, despite the longer lead time, the correlation values are slightly larger in July than September. This increased correlation is directly related to the primary finding of this paper: Arctic sea ice volume anomalies tend to be enhanced over the summer months, peaking in July.

Computing a volume anomaly time series for the control simulation, we have identified high- and low-volume states, and studied the conditional evolution of volume anomalies in these states. There is a clear seasonality to the high- and low-volume event count, with a greater prevalence of high- and low-volume events over the summer months. The volume anomaly evolution shows a clear summer enhancement, in which anomalies grow between the months of May and July because of a positive ice–albedo feedback mechanism. A typical summer volume anomaly enhancement in a high- or low-volume state corresponds to a spatially averaged SIT anomaly of 7 cm over the September-ice zone. We have found that the summer volume anomaly enhancement is robust with respect to the initial month, as anomalies present in different initial months exhibit a similar volume evolution. In particular, the volume anomaly enhancement in both high- and low-volume states consistently peaks in July. It is crucial to note that the summer volume anomaly enhancement is a statistical feature and individual events exhibit a significant amount of internal variability. Typically, the anomaly enhancement can be robustly identified when averaging over 10 (or more) randomly selected high- and low-volume years, which is similar to a typical forecast ensemble size. We have also found that the size of the summer volume anomaly enhancement increases monotonically with the size of the initial volume anomaly, indicating that this phenomenon is always present but most significant in large anomaly years. The summer SIT enhancement has a spatially broad signal that encompasses most of the September-ice zone, with SIT anomalies that persist throughout the year and are largest in July, August, and September. The SIC field is characterized by an annular anomaly pattern surrounding the perennial-ice zone, with matching sign to the SIT anomalies.

Analysis of the surface energy budget in high- and low-volume states revealed that the summer volume enhancement is primarily driven by anomalies in absorbed shortwave radiation (SW) over the months of May–July. The anomalous SW energy input corresponds closely to the observed changes in ice thickness. Following the volume enhancement, which peaks in July, there is an SIC anomaly that peaks in September and latent and sensible heat flux (LH + SH) anomalies that peak in October. Owing to the persistence of SIT anomalies, this sequence of events repeats in subsequent years, with SW, SIC, and LH + SH anomaly amplitudes that scale with the size of the SIT anomaly. We have found that SIT anomalies have e-folding time scales of 4.6 and 3.1 yr in high- and low-volume states, respectively. These time scales also set the decay time scale for the summer enhancement phenomenon and related variables in the surface energy budget. We have demonstrated that the SW anomalies result from SIT-state-dependent changes in surface albedo. These albedo changes are driven by SIC and surface properties related to the melt-onset date and snow coverage in May and June, and by anomalies in SIC in July and August. A schematic summary of the mechanism for summer volume anomaly enhancement is provided in Fig. 11b.

It is interesting to note that a similar volume enhancement also occurs in the context of initialized forecast ensembles with perturbed SIT initial conditions. Since the sole change to the initial conditions was SIT, this directly attributes the volume enhancement to the SIT state. The results of this study suggest that future initialization strategies incorporating SIT, SIC, and surface melt ponds may be promising for seasonal forecasting systems since each of these have an important influence on the ice–albedo feedback. These findings highlight the need for accurate representation of the ice–albedo feedback in GCMs since its strength crucially affects summer SIT and September sea ice extent. Future work testing the robustness of the conclusions of this study across other GCMs, especially those with explicit representation of melt ponds, is needed.

Acknowledgments. We thank A. Stern, R. Zhang, and three anonymous reviewers for helpful comments and suggestions, which improved the manuscript. This study was supported by NOAA's Climate Program Office, Climate Variability and Predictability Program (Award GC15-504). We thank C. Raphael for assistance with Fig. 11.

APPENDIX

Detailed Methodology

a. Computation of transmitted surface energy fluxes

We estimate transmitted shortwave radiation (SWT) using monthly averaged data of snow depth h_s, ice-category concentrations c_i, and absorbed shortwave radiation SW. This estimate has potential errors for two reasons: 1) the thicknesses in each ice category h_i are not saved for this run and need to be estimated, and 2) h_s, c_i, and SW are saved at monthly time resolution. Since SWT is based on instantaneous products of these quantities, using monthly averaged data may introduce biases. In particular, since 1 − SIC and SW have a positive covariance, our estimate is likely an underestimate of the true transmitted shortwave radiation.

A portion of SW is directly absorbed by the ocean surface and a portion is transmitted through sea ice, according to Beer's law. We let $\mathrm{SW}_{\mathrm{ocean}}$ be the net shortwave radiation that is absorbed by the ocean surface. Note that, because of the presence of sea ice, $\mathrm{SW}_{\mathrm{ocean}} \le \mathrm{SW}$. Let I_0 be the amount of SW that penetrates into the ice. The term I_0 is given by

$$I_0 = 0.3(1 - f_{\mathrm{snow}})\mathrm{SW}, \tag{A1}$$

where

$$f_{\mathrm{snow}} = \frac{h_s}{h_s + 0.02} \tag{A2}$$

and h_s is the snow depth. The SW penetration is given by

$$I(z) = I_0 e^{-\kappa z}, \tag{A3}$$

where $\kappa = 1/0.67\,\mathrm{m}^{-1}$ is the extinction coefficient. Therefore, $\mathrm{SW}_{\mathrm{ocean}}$ is given by

$$\mathrm{SW}_{\mathrm{ocean}} = \sum_{k=1}^{5} I(h_i)c_i + \left(1 - \sum_{k=1}^{5} c_i\right)\mathrm{SW}. \quad \text{(A4)}$$

The first term represents the amount of SW that penetrates through sea ice, and the second term represents the SW absorbed directly by the ocean (through leads and in ice-free regions). To compute the first term, we need h_i, which is not saved as an output variable for this run. However, we do have c_i, and we know the thickness category limits. We choose to estimate the h_i values as the midpoint of each thickness category. Specifically, we use the following values: $h_1 = 0.05$, $h_2 = 0.2$, $h_3 = 0.5$, $h_4 = 0.9$, and $h_5 = 2$. With this choice, we can compute $\mathrm{SW}_{\mathrm{ocean}}$.

Finally, we want to compare $\mathrm{SW}_{\mathrm{ocean}}$ to F_{ocean}, the total ice–ocean heat flux. Since F_{ocean} is only defined over grid points with positive SIC, we weight $\mathrm{SW}_{\mathrm{ocean}}$ by SIC to allow for a proper comparison. We define SWT as

$$\mathrm{SWT} = \mathrm{SW}_{\mathrm{ocean}} \times \mathrm{SIC}. \quad \text{(A5)}$$

Therefore, SWT represents the shortwave flux into the ocean surface in the ice-covered regions of the Arctic. We follow a similar procedure, without the Beer's Law contribution in Eq. (A4), to compute the transmitted fluxes from the other terms in the surface energy budget.

b. Modification of sea ice thickness initial conditions

Here we describe the construction of the SIT initial conditions for the $\mathrm{FLOR}_{\mathrm{SITpert}}$ experiments. Let $H(x, y, t)$ be the SIT in the ice-covered portion of the grid cell, defined as

$$H = \frac{\sum_i c_i h_i}{\sum_i c_i}, \quad \text{(A6)}$$

where h_i and c_i are the thickness and concentration in the ith ice-thickness category. Let $H_{\mathrm{FLOR}}(x, y, t)$ and $H_{\mathrm{IC}}(x, y, t)$ be the SIT fields from historical runs of FLOR and ECDA, respectively. Let the overbar indicate a time averaging performed over the FLOR hindcast prediction period (1982–2014). We would like to create a set of perturbed SIT initial conditions $\tilde{H}_{\mathrm{IC}}$, defined at each grid point by

$$\tilde{H}_{\mathrm{IC}}(x,y,t) = H_{\mathrm{IC}}(x,y,t) + \Delta H(x,y), \quad \text{(A7)}$$

where

$$\Delta H(x,y) = \overline{H_{\mathrm{FLOR}}(x,y,t)} - \overline{H_{\mathrm{IC}}(x,y,t)}. \quad \text{(A8)}$$

We now compute a multiplicative scaling factor $1 + \lambda$, which, when applied to each h_i, will yield the desired perturbation in H. We choose this multiplicative scaling technique instead of an additive shift because the multiplicative scaling provides better fidelity to the ice thickness distribution, which is important for the simulation of many aspects of polar climate (Holland et al. 2006). In the present case, ΔH is typically 1 m in the central Arctic. Therefore, an additive shift would effectively place all ice into thickness category 5, which would introduce systematic thermodynamic, dynamic, and albedo biases (Holland et al. 2006). We define $\lambda(x, y, t)$ as

$$\lambda(x,y,t) = \frac{\overline{H_{\mathrm{FLOR}}(x,y,t)} - \overline{H_{\mathrm{IC}}(x,y,t)}}{H_{\mathrm{IC}}(x,y,t)}. \quad \text{(A9)}$$

Next we scale the original initial conditions in each thickness category by a multiplicative factor of $1 + \lambda$:

$$\tilde{H}_{\mathrm{IC}}(x,y,t) = \frac{\sum_i c_i h_i (1+\lambda)}{\sum_i c_i} = (1+\lambda)H_{\mathrm{IC}}(x,y,t)$$
$$= H_{\mathrm{IC}}(x,y,t) + \Delta H(x,y), \quad \text{(A10)}$$

which yields the desired thickness perturbation.

This methodology can break down when 1) $|\Delta H| > 0$ and $H_{\mathrm{IC}} = 0$ (adding ice to an ice-free grid point) or 2) when $1 + \lambda \le 0$ (removing ice from an ice-covered grid point). To avoid model instabilities associated with these, we incorporate two additional criteria:

1) The SIT correction is only applied to grid points where $H_{\mathrm{IC}} \ge 0.1$ m.
2) If $1 + \lambda < 1$, the ice can only be thinned to a minimum of 0.1 m (i.e., ice cannot be completely removed by this procedure).

These two criteria, which are primarily applied near the sea ice edge, are sufficient for the model to run stably with the new SIT initial conditions.

REFERENCES

Bitz, C., M. Holland, A. Weaver, and M. Eby, 2001: Simulating the ice-thickness distribution in a coupled climate model. *J. Geophys. Res.*, **106**, 2441–2463, doi:10.1029/1999JC000113.

Blanchard-Wrigglesworth, E., K. C. Armour, C. M. Bitz, and E. DeWeaver, 2011a: Persistence and inherent predictability of Arctic sea ice in a GCM ensemble and observations. *J. Climate*, **24**, 231–250, doi:10.1175/2010JCLI3775.1.

——, C. Bitz, and M. Holland, 2011b: Influence of initial conditions and climate forcing on predicting Arctic sea ice. *Geophys. Res. Lett.*, **38**, L18503, doi:10.1029/2011GL048807.

——, R. Cullather, W. Wang, J. Zhang, and C. Bitz, 2015: Model forecast skill and sensitivity to initial conditions in the seasonal sea ice outlook. *Geophys. Res. Lett.*, **42**, 8042–8048, doi:10.1002/2015GL065860.

Budyko, M., 1969: The effect of solar radiation variations on the climate of the earth. *Tellus*, **21A**, 611–619, doi:10.1111/j.2153-3490.1969.tb00466.x.

Bushuk, M., and D. Giannakis, 2015: Sea-ice reemergence in a model hierarchy. *Geophys. Res. Lett.*, **42**, 5337–5345, doi:10.1002/2015GL063972.

——, ——, and A. J. Majda, 2014: Reemergence mechanisms for North Pacific sea ice revealed through nonlinear Laplacian spectral analysis. *J. Climate*, **27**, 6265–6287, doi:10.1175/JCLI-D-13-00256.1.

——, ——, and ——, 2015: Arctic sea-ice reemergence: The role of large-scale oceanic and atmospheric variability. *J. Climate*, **28**, 5477–5509, doi:10.1175/JCLI-D-14-00354.1.

Chevallier, M., and D. Salas y Mélia, 2012: The role of sea ice thickness distribution in the Arctic sea ice potential predictability: A diagnostic approach with a coupled GCM. *J. Climate*, **25**, 3025–3038, doi:10.1175/JCLI-D-11-00209.1.

——, ——, A. Voldoire, M. Déqué, and G. Garric, 2013: Seasonal forecasts of the pan-Arctic sea ice extent using a GCM-based seasonal prediction system. *J. Climate*, **26**, 6092–6104, doi:10.1175/JCLI-D-12-00612.1.

Collow, T. W., W. Wang, A. Kumar, and J. Zhang, 2015: Improving Arctic sea ice prediction using PIOMAS initial sea ice thickness in a coupled ocean–atmosphere model. *Mon. Wea. Rev.*, **143**, 4618–4630, doi:10.1175/MWR-D-15-0097.1.

Curry, J. A., J. L. Schramm, and E. E. Ebert, 1995: Sea ice–albedo climate feedback mechanism. *J. Climate*, **8**, 240–247, doi:10.1175/1520-0442(1995)008<0240:SIACFM>2.0.CO;2.

Day, J., E. Hawkins, and S. Tietsche, 2014a: Will Arctic sea ice thickness initialization improve seasonal forecast skill? *Geophys. Res. Lett.*, **41**, 7566–7575, doi:10.1002/2014GL061694.

——, S. Tietsche, and E. Hawkins, 2014b: Pan-Arctic and regional sea ice predictability: Initialization month dependence. *J. Climate*, **27**, 4371–4390, doi:10.1175/JCLI-D-13-00614.1.

Delworth, T. L., and Coauthors, 2006: GFDL'S CM2 global coupled climate models. Part I: Formulation and simulation characteristics. *J. Climate*, **19**, 643–674, doi:10.1175/JCLI3629.1.

——, and Coauthors, 2012: Simulated climate and climate change in the GFDL CM2. 5 high-resolution coupled climate model. *J. Climate*, **25**, 2755–2781, doi:10.1175/JCLI-D-11-00316.1.

DeRepentigny, P., B. Tremblay, R. Newton, and S. Pfirman, 2016: Patterns of sea-ice retreat in the transition to a seasonally ice-free Arctic. *J. Climate*, **29**, 6993–7008, doi:10.1175/JCLI-D-15-0733.1.

Germe, A., M. Chevallier, D. Salas y Mélia, E. Sanchez-Gomez, and C. Cassou, 2014: Interannual predictability of Arctic sea ice in a global climate model: Regional contrasts and temporal evolution. *Climate Dyn.*, **43**, 2519–2538, doi:10.1007/s00382-014-2071-2.

Guemas, V., M. Chevallier, M. Dqu, O. Bellprat, and F. Doblas-Reyes, 2016: Impact of sea ice initialization on sea ice and atmosphere prediction skill on seasonal timescales. *Geophys. Res. Lett.*, **43**, 3889–3896, doi:10.1002/2015GL066626.

Holland, M. M., and C. M. Bitz, 2003: Polar amplification of climate change in coupled models. *Climate Dyn.*, **21**, 221–232, doi:10.1007/s00382-003-0332-6.

——, and J. Stroeve, 2011: Changing seasonal sea ice predictor relationships in a changing Arctic climate. *Geophys. Res. Lett.*, **38**, L18501, doi:10.1029/2011GL049303.

——, C. Bitz, E. Hunke, W. Lipscomb, and J. Schramm, 2006: Influence of the sea ice thickness distribution on polar climate in CCSM3. *J. Climate*, **19**, 2398–2414, doi:10.1175/JCLI3751.1.

——, D. A. Bailey, and S. Vavrus, 2011: Inherent sea ice predictability in the rapidly changing Arctic environment of the Community Climate System Model, version 3. *Climate Dyn.*, **36**, 1239–1253, doi:10.1007/s00382-010-0792-4.

Hunke, E., and J. Dukowicz, 1997: An elastic–viscous–plastic model for sea ice dynamics. *J. Phys. Oceanogr.*, **27**, 1849–1867, doi:10.1175/1520-0485(1997)027<1849:AEVPMF>2.0.CO;2.

——, W. H. Lipscomb, A. K. Turner, N. Jeffery, and S. Elliot, 2015: CICE: The Los Alamos sea ice model documentation and software user's manual version 5.1. Los Alamos National Laboratory Rep. LA-CC-06-012, 116 pp.

Jung, T., and Coauthors, 2016: Advancing polar prediction capabilities on daily to seasonal time scales. *Bull. Amer. Meteor. Soc.*, **97**, 1631–1647, doi:10.1175/BAMS-D-14-00246.1.

Kaleschke, L., X. Tian-Kunze, N. Maaß, M. Mäkynen, and M. Drusch, 2012: Sea ice thickness retrieval from *SMOS* brightness temperatures during the Arctic freeze-up period. *Geophys. Res. Lett.*, **39**, L05501, doi:10.1029/2012GL050916.

Koenigk, T., and U. Mikolajewicz, 2009: Seasonal to interannual climate predictability in mid and high northern latitudes in a global coupled model. *Climate Dyn.*, **32**, 783–798, doi:10.1007/s00382-008-0419-1.

Laxon, S. W., and Coauthors, 2013: Cryosat-2 estimates of Arctic sea ice thickness and volume. *Geophys. Res. Lett.*, **40**, 732–737, doi:10.1002/grl.50193.

Lemke, P., E. Trinkl, and K. Hasselmann, 1980: Stochastic dynamic analysis of polar sea ice variability. *J. Phys. Oceanogr.*, **10**, 2100–2120, doi:10.1175/1520-0485(1980)010<2100:SDAOPS>2.0.CO;2.

Lindsay, R., and Coauthors, 2012: Seasonal forecasts of Arctic sea ice initialized with observations of ice thickness. *Geophys. Res. Lett.*, **39**, L21502, doi:10.1029/2012GL053576.

Liu, J., M. Song, R. M. Horton, and Y. Hu, 2015: Revisiting the potential of melt pond fraction as a predictor for the seasonal Arctic sea ice extent minimum. *Environ. Res. Lett.*, **10**, 054017, doi:10.1088/1748-9326/10/5/054017.

Merryfield, W., W.-S. Lee, W. Wang, M. Chen, and A. Kumar, 2013: Multi-system seasonal predictions of Arctic sea ice. *Geophys. Res. Lett.*, **40**, 1551–1556, doi:10.1002/grl.50317.

Msadek, R., G. Vecchi, M. Winton, and R. Gudgel, 2014: Importance of initial conditions in seasonal predictions of Arctic sea ice extent. *Geophys. Res. Lett.*, **41**, 5208–5215, doi:10.1002/2014GL060799.

Perovich, D. K., and C. Polashenski, 2012: Albedo evolution of seasonal Arctic sea ice. *Geophys. Res. Lett.*, **39**, L08501, doi:10.1029/2012GL051432.

——, S. V. Nghiem, T. Markus, and A. Schweiger, 2007: Seasonal evolution and interannual variability of the local solar energy absorbed by the Arctic sea ice–ocean system. *J. Geophys. Res.*, **112**, C03005, doi:10.1029/2006JC003558.

Peterson, K. A., A. Arribas, H. Hewitt, A. Keen, D. Lea, and A. McLaren, 2015: Assessing the forecast skill of Arctic sea ice extent in the GloSea4 seasonal prediction system. *Climate Dyn.*, **44**, 147–162, doi:10.1007/s00382-014-2190-9.

Rigor, I. G., and J. M. Wallace, 2004: Variations in the age of Arctic sea-ice and summer sea-ice extent. *Geophys. Res. Lett.*, **31**, L09401, doi:10.1029/2004GL019492.

Schröder, D., D. L. Feltham, D. Flocco, and M. Tsamados, 2014: September Arctic sea-ice minimum predicted by spring melt-pond fraction. *Nat. Climate Change*, **4**, 353–357, doi:10.1038/nclimate2203.

Screen, J. A., and I. Simmonds, 2013: Exploring links between Arctic amplification and mid-latitude weather. *Geophys. Res. Lett.*, **40**, 959–964, doi:10.1002/grl.50174.

Serreze, M. C., A. P. Barrett, A. G. Slater, M. Steele, J. Zhang, and K. E. Trenberth, 2007: The large-scale energy budget of the Arctic. *J. Geophys. Res.*, **112**, D11122, doi:10.1029/2006JD008230.

Sigmond, M., J. Fyfe, G. Flato, V. Kharin, and W. Merryfield, 2013: Seasonal forecast skill of Arctic sea ice area in a dynamical forecast system. *Geophys. Res. Lett.*, **40**, 529–534, doi:10.1002/grl.50129.

Stroeve, J., V. Kattsov, A. Barrett, M. Serreze, T. Pavlova, M. Holland, and W. N. Meier, 2012: Trends in Arctic sea ice extent from CMIP5, CMIP3 and observations. *Geophys. Res. Lett.*, **39**, L16502, doi:10.1029/2012GL052676.

——, L. C. Hamilton, C. M. Bitz, and E. Blanchard-Wrigglesworth, 2014a: Predicting September sea ice: Ensemble skill of the SEARCH sea ice outlook 2008–2013. *Geophys. Res. Lett.*, **41**, 2411–2418, doi:10.1002/2014GL059388.

——, T. Markus, L. Boisvert, J. Miller, and A. Barrett, 2014b: Changes in Arctic melt season and implications for sea ice loss. *Geophys. Res. Lett.*, **41**, 1216–1225, doi:10.1002/2013GL058951.

Tietsche, S., and Coauthors, 2014: Seasonal to interannual Arctic sea ice predictability in current global climate models. *Geophys. Res. Lett.*, **41**, 1035–1043, doi:10.1002/2013GL058755.

Tilling, R. L., A. Ridout, A. Shepherd, and D. J. Wingham, 2015: Increased Arctic sea ice volume after anomalously low melting in 2013. *Nat. Geosci.*, **8**, 643–646, doi:10.1038/ngeo2489.

Vecchi, G. A., and Coauthors, 2014: On the seasonal forecasting of regional tropical cyclone activity. *J. Climate*, **27**, 7994–8016, doi:10.1175/JCLI-D-14-00158.1.

Walsh, J. E., and C. M. Johnson, 1979: An analysis of Arctic sea ice fluctuations, 1953–77. *J. Phys. Oceanogr.*, **9**, 580–591, doi:10.1175/1520-0485(1979)009<0580:AAOASI>2.0.CO;2.

Wang, W., M. Chen, and A. Kumar, 2010: An assessment of the CFS real-time seasonal forecasts. *Wea. Forecasting*, **25**, 950–969, doi:10.1175/2010WAF2222345.1.

——, ——, and ——, 2013: Seasonal prediction of Arctic sea ice extent from a coupled dynamical forecast system. *Mon. Wea. Rev.*, **141**, 1375–1394, doi:10.1175/MWR-D-12-00057.1.

Williams, J., B. Tremblay, R. Newton, and R. Allard, 2016: Dynamic preconditioning of the minimum September sea-ice extent. *J. Climate*, **29**, 5879–5891, doi:10.1175/JCLI-D-15-0515.1.

Winton, M., 2000: A reformulated three-layer sea ice model. *J. Atmos. Oceanic Technol.*, **17**, 525–531, doi:10.1175/1520-0426(2000)017<0525:ARTLSI>2.0.CO;2.

——, 2006: Amplified Arctic climate change: What does surface albedo feedback have to do with it? *Geophys. Res. Lett.*, **33**, L03701, doi:10.1029/2005GL025244.

Yang, Q., S. N. Losa, M. Losch, X. Tian-Kunze, L. Nerger, J. Liu, L. Kaleschke, and Z. Zhang, 2014: Assimilating *SMOS* sea ice thickness into a coupled ice-ocean model using a local SEIK filter. *J. Geophys. Res. Oceans*, **119**, 6680–6692, doi:10.1002/2014JC009963.

Zhang, R., 2015: Mechanisms for low-frequency variability of summer Arctic sea ice extent. *Proc. Natl. Acad. Sci. USA*, **112**, 4570–4575, doi:10.1073/pnas.1422296112.

Zhang, S., M. Harrison, A. Rosati, and A. Wittenberg, 2007: System design and evaluation of coupled ensemble data assimilation for global oceanic climate studies. *Mon. Wea. Rev.*, **135**, 3541–3564, doi:10.1175/MWR3466.1.